ISSN: 2830-8603

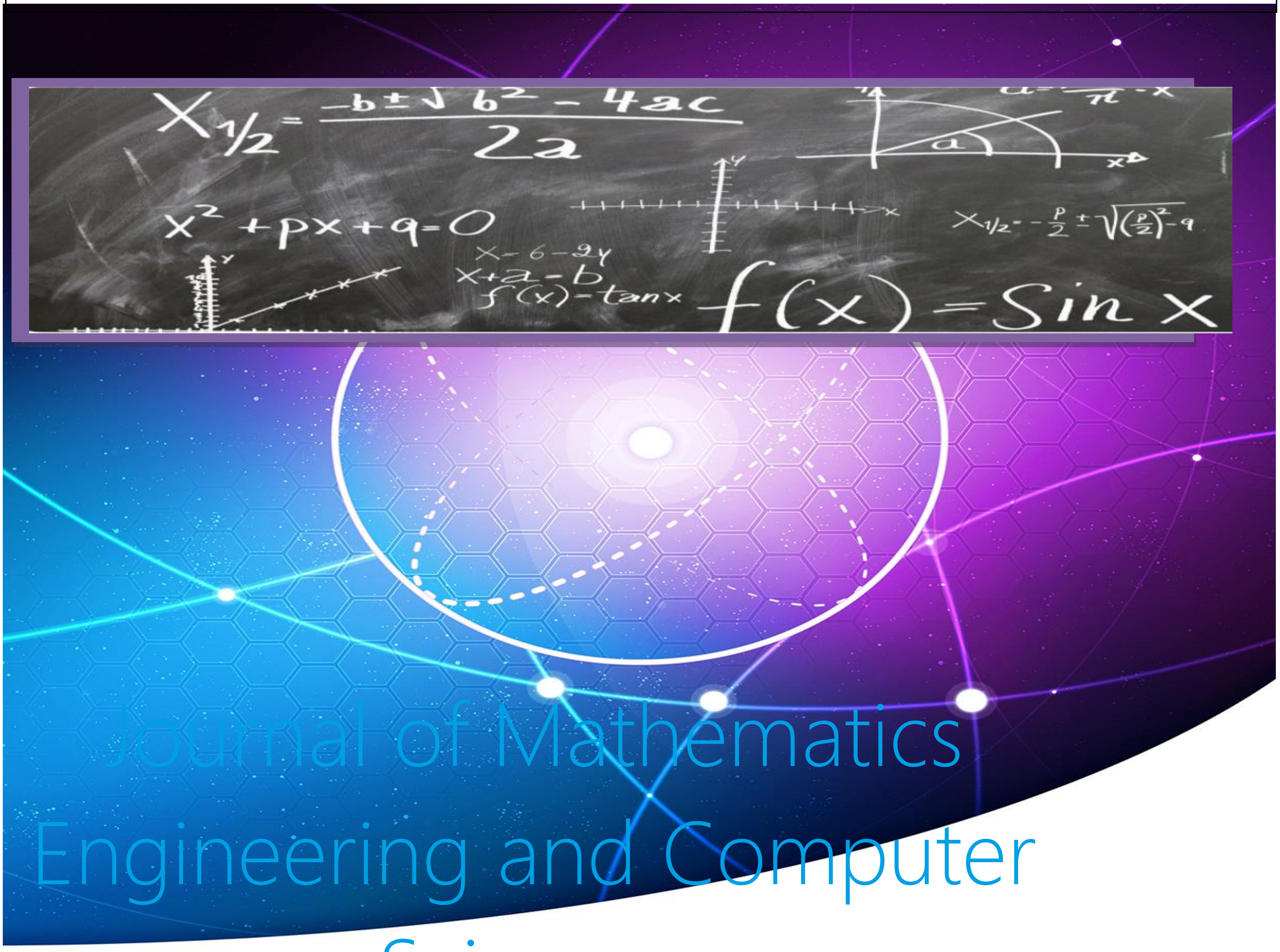

Journal of Mathematics Engineering and Computer Sciences

Khenchela University Scientific Publication

Journal of
Mathematics, Engineering and Computer Sciences (JMEC)

Volume 0000, No. 0000, Month July, Year 2024

Khenchela University Scientific Publications

Editorial Board

Associate Editors

Instructions to authors

Editorial policy

The Journal of Mathematics, Engineering and Computer Sciences (JMEC)) is an open-access peer-reviewed journal devoted to publishing original papers of high technical standards with a suitable balance of practice and theory related to the broad topics in the field of Mathematics, Engineering and Computer Sciences.

JMEC is a scientific journal published twice a year at Khenchela University, Algeria. The aim is to feature a wide variety of research areas and to bring to the community the latest developments in mathematical sciences, Engineering and the computer sciences. Submissions from any part of the world are welcomed.

Review Process:

JMEC operates a single-blind review process. All submitted manuscripts will be initially assessed by the editor-in-chief for suitability for the journal. Papers deemed suitable are then typically sent to a minimum of two independent expert reviewers to assess the scientific quality of the paper. The Editor is responsible for the final decision regarding acceptance or rejection of articles. In so doing, JMEC needs reviewers who can provide insightful and helpful comments on submitted manuscripts with a turnaround time of about 4 weeks. Maintaining JMEC as a scientific journal of high quality depends on reviewers with a high level of expertise and an ability to be objective, fair, and insightful in their evaluation of manuscripts.

Plagiarism Policy:

The JMEC checks the plagiarism of the submitted manuscript by a plagiarism checker software before the peer-review process. However, if the plagiarism of a manuscript is proved after publication, the JMEC can reject the paper. According to the JMEC policies, the similarity of the submitted manuscript should be less than 20 percent. Plagiarism can take several forms, including but not limited to:

- ✓ Using the exact words of another author in part of a paper without both citation and quotation marks;
- ✓ Including the paraphrased or summarized idea of another author without acknowledging its source;
- ✓ Cutting and pasting material from Internet or other electronic resources without proper citation of sources;
- ✓ Writing a computer program that is the same or closely similar to existing sources.

Self-Archiving Policy:

Authors who submit their manuscript in JMEC can share their research at any time after the acceptance.

Submission of papers

Authors are encouraged to submit manuscripts as E-mail attachments to the editor in chief (jmec@univ-khenchela.dz). Manuscripts must be accompanied by a cover page stating the title, name(s), postal address, telephone and fax numbers (if any) and e-mail addresses of the authors of the paper. Alternatively, authors can also send three hard copies of their paper together with a cover page to: Editor-in-Chief, Journal of Mathematics, Engineering and Computer Sciences, Faculty of Sciences and Technologies, Abbes Laghrour University, Khenchela, BP 1252 Road of Batna, 40004, Algeria. Hard copies should be accompanied by a CD. No manuscripts submitted should have been published or are under consideration for publication elsewhere.

After acceptation of the paper, all manuscripts should be typed on one side of the paper using a word processing program such as MS word.

Abstracts and subject of classification (if it exists) should be given. Equations, chemical formulas, tables and figures should be numbered.

References should be cited in the text by numbers between square brackets like [1], [2, P. 161] .

[1] Q. Liang, N. N. Karnik, and J. M. Mendel, “Connection admission control in ATM networks using survey-based type-2 fuzzy logic systems,” *IEEE Transactions Systems*, Vol.30, No. 3, pp. 329–339, 2000.

[2] P.Cesar da Silva, D.dos Santos Matos, A. Nied, M. Santos Matos Cavalca, J.Oliveira,’’ Reduction of synchronous reluctance motor currents with minimization of direct and cross saturation magnetic model, ISA Transactions 111 (2021) 223–230

[3] G.Boztas, O. Aydogmus, “ Implementation of sensorless speed control of synchronous reluctance motor using extended Kalman filter,” doi.org/10.1016/j.jestch.2021.09.012.

[4] Fliess M, Lévine J, Martin P, Rouchon P (2007) Flatness and defect of non-linear systems, introductory theory and examples. Int J Control 61(6):1327–1361.

Proof reading

Prior to publication a set of proofs of each article will be sent to the corresponding authors. Authors are asked to correct and return their final revised manuscript as well as the originals of figures to the Editor-in-Chief at the above address.

(JMECS) J. Math. Eng. Comp. Sc.
Vol. 00, No. 00, pp. 1-10, (July 2024-Safar 1445$_H$)
© Abbes Laghrour Khenchela University Publications

Sensorless Speed Control of Synchronous Variable Reluctance Motordrive using DTC and MRAS Observer

Beddiaf Yassine[a,b] and Laggoun Louanasse[a,b]

[a] University Abbes Laghrour, Khenchela, Algeria.

E-mail: beddiaf.yassine@univ-khenchela.dz

[b] LSTEB Laboratory, University of Batna-2, Algeria.
E-mail: laggounsamir@yahoo.fr

Abstract*:*In this paper we present the sensorless speed control of synchronous variable reluctance motor using the direct torque control technique (DTC) and SM-MRAS observer. This observer is used to estimate speed and stator flux. As we know that the classical MRAS observer consists essentially of two models, the first represents the reference model and the second represents the adjustable model. But the mathematical model of our machine in the (dq) reference frame is based on a single system of stator electrical equations. Therefore, we propose the MRAS observer, this observer is based on the only stator model..The obtained simulation results confirm the feasibility of sensorless control of SynRVM.

Keywords*:* Sensorless control, Synchronous variable reluctance motor (SynVRM); Direct Torque Control (DTC); MRAS.

AMS Classification:

I. Introduction

The synchronous variable reluctance motor (SynVRM) has many advantages than other ac motors. For example, large speed variation ranges. Moreover, its rotor doesnot have any winding or magnetic material; it is similar to that of an induction motor.Recently, many researchershave proposed several control methods to improve theperformance of drive system. Infact, the SRM has been shown to be suitable for ac drivesystems for several reasons. For example, it is notnecessary to compute the slip of SynVRM as with induction motor. Moreover, the rotor speed depends on the frequency of stator current, and the control system is simple and reliable.

As a result, there is no rotor parametersensitivity problem. Furthermore, it does not require anyexcitation winding and permanent magnet as the classicalsynchronous motor.In this context, many contributions have been proposed to improve the performance of SynVRM control [4-15].In[3] the authors have proposed a sensorless synchronous reluctance motor drives based on a full-speed scheme using predictive control technique based on a finite-control-Set model. In [4]Tian-Hua Liu and Hsiao-Hao Hsuproposed an Adaptive Controller Design for a Synchronous Reluctance Motor with Direct Torque Control, two controller types namelyan adaptive backstepping controller and a model-reference adaptive controller, are proposed and the results are compared with those obtained by a PI controller, the findings are almost the same.The reference [5] proposeda PI current-loop controller anda predictive speed-loop controller. In [6] a comprehensive performance comparison has been made for different methods of constant current angle vector control, including MTPA (Maximum torque per ampere), MPFC (Maximum power factor control) and MTPF (Maximum torque per flux).In [7] the authors have proposeda solution to improve the control performance based on asimplified modulated model predictive control (SMMPC), this method is applied to the synchronous reluctance motor. Also, SMMPC method simplifies the previous MMPCmethod by simplifying the cost functions. The voltages are used in the cost function instead of the motor currents in thestationary reference frame. Therefore, this simplification results in saving computation timecompared to the MMPC.

In [8], a rotor position estimator has beenimplemented based on the measurement of the rate change in stator currents, the authorsshow that their method performs well at a low-speed. However, the estimation position deteriorates as the speed of the motor increaseswhich needs the addition of a compensator. In realty, the latter is related to the motor speeds and initial currents. Furthermore, the compensator has three-dimensional, which makes his design a difficult task.

The authors of [9] Propose a modified second-order sliding mode control combined with radial basis functionnetwork estimatorfor speed tracking in synchronous reluctance motor, the obtained results seem very satisfactory but the oscillation problem still persists. In article[10], the authors propose a novel online adaptive observer algorithm for the SynRM, which can provide the position and speed information required for sensorless operation, they used the Kalman filter as an observer.

In this paper, we propose a sensorless DTC control based on the MRAS observer.The simulation results obtained prove that excellent control performance is shown to be possible, which indicates that SynVRM can be suitably applied to high performance drive systems, perhaps even exceed that of induction motor.

II. Mathematical model of SVRM

In SVRM, high permeability path is referred to direct d-axis path, while the low permeability steering is referred to quadrature q-axis steering, as shown in Fig. 1.As in synchronous variable reluctancemotor (SVRM), the maximum flux is located on the d-axis while the flux on the q-axis is limited by the rotor barriers [2].

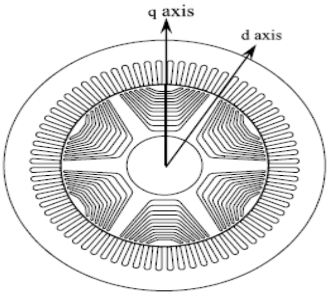

Fig.1 Example of structure of SynVRM.

Fig.2 shows the windings of the machine in the two-phase reference system.The voltage equationsof the SynVRMin synchronous d-q reference frame(rotating rotor d-q reference frame) can bewritten as:

$$\begin{cases} V_{ds} = R_s i_{ds} + \dfrac{d\varphi_{ds}}{dt} - \omega\varphi_{qs} \\ V_{qs} = R_s i_{qs} + \dfrac{d\varphi_{qs}}{dt} + \omega\varphi_{ds} \\ 0 = R_r i_{dr} + \dfrac{d\varphi_{dr}}{dt} \\ 0 = R_r i_{qr} + \dfrac{d\varphi_{qr}}{dt} \end{cases} \qquad (1)$$

The flux linkage equations are:

$$\begin{cases} \varphi_{ds} = L_d i_{ds} + M_d i_{dr} \\ \varphi_{qs} = L_q i_{qs} + M_q i_{qr} \\ \varphi_{dr} = L_d i_{dr} + M_d i_{ds} \\ \varphi_{qs} = L_d i_{qr} + M_d i_{qs} \end{cases}$$

□□□□□□□□□□□□□

□□□□□

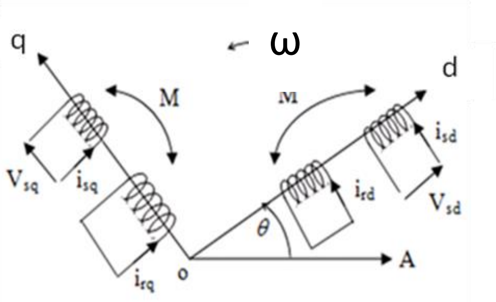

Fig.2. Winding representation of SVRM in dq reference

Where V_{ds} and V_{qs} are the d-axis and q-axis voltages, R_s is the stator resistance, i_{ds} is the direct current, i_{qs} is the quadratic current, φ_{ds} and φ_{qs} are the d-axis and q-axis flux linkages, ω is the rotor speed. L_d isthe d-axis inductance, L_q is the q-axis inductance, M_d is the d-axis mutual inductance, M_q is the q-axis mutual inductance.

By handlingequations (1) and (2), we obtain the following flux model:

$$\begin{cases} \dfrac{di_{ds}}{dt} = -\dfrac{R_s}{L_d} i_{ds} + \omega \dfrac{L_q}{L_d} i_{qs} + \dfrac{1}{L_d} V_{ds} \\ \dfrac{di_{qs}}{dt} = -\dfrac{R_s}{L_q} i_{qs} - \omega \dfrac{L_d}{L_q} i_{ds} + \dfrac{1}{L_q} V_{qs} \end{cases} \qquad (3)$$

The electromagnetic torque can be expressed as

$$T_e = \frac{3p}{2}(\varphi_{ds} i_{qs} - \varphi_{qs} i_{ds}) \; (4)$$

Where T_e is the electromagnetic torque of the motor, p is the number of poles of the motor.

The rotor speedand position of the motor can be expressed as

$$\frac{d\omega_r}{dt} = \frac{1}{J}\left(T_e - T_l - f\omega_r\right) \qquad (5)$$

and

$$\frac{d\theta}{dt} = \omega_r \qquad (6)$$

where J is the inertia constant of the motor and load, T_l is the external load torque, f is the viscous frictionalcoefficient of the motor and load, θ is the mechanical rotor position, and ω is the mechanical rotor speed.

III.Direct Torque Control (DTC) of SVRM

The direct torque control of SVRM is essentially based on the direct determination of control sequences of the inverter, i.e. there is no need for the PWM modulator. The torque of synchronous variable reluctance motoris controlled by monitoring and controlling the armature current since electromagnetic torque is proportional to the this current.From equation (3) we can say that in DTC, torque and flux can be controlled independently since the stator flux is controlled directly withthe stator voltage using equations (7) and (8). Moreover, torque is estimated by using current data provided by equation (9).

$$\varphi_\alpha = \int_t^{t+\Delta t} \left(V_\alpha - R_s i_{\alpha s}\right) dt \qquad (7)$$

$$\varphi_\beta = \int_t^{t+\Delta t} \left(V_\beta - R_s i_{\beta s}\right) dt \qquad (8)$$

$$\hat{T}_e = \frac{3p}{2}\left(\varphi_{\alpha s} i_{\beta s} - \varphi_{\beta s} i_{\alpha s}\right) \qquad (9)$$

Each of the three arms of the inverter is either at the High level ($S_j = 1$)or the Low level ($S_j = 0$), so the arm potential (j) is $S_j U_{dc}$, where $j = a,b,c$, in this case the voltages generated by the inverter are:

$$\begin{bmatrix} V_a \\ V_b \\ V_c \end{bmatrix} = U_{dc} \cdot \begin{bmatrix} \frac{2}{3} & -\frac{1}{3} & -\frac{1}{3} \\ -\frac{1}{3} & \frac{2}{3} & -\frac{1}{3} \\ -\frac{1}{3} & -\frac{1}{3} & \frac{2}{3} \end{bmatrix} \cdot \begin{bmatrix} S_a \\ S_b \\ S_c \end{bmatrix}$$

(10)

These voltages in Clark's d-q reference frame (fixed reference frame) are given by:

$$\begin{pmatrix} V_{\alpha s} \\ V_{\beta s} \end{pmatrix} = \begin{pmatrix} U_{dc}\sqrt{\frac{2}{3}}\left(S_a - \frac{1}{2}\left(S_b + S_c\right)\right) \\ \frac{1}{\sqrt{2}} U_{dc}\left(S_b - S_c\right) \end{pmatrix}$$

(11)

Voltage vector for the DTC is determined by comparing the estimated stator flux and torque values with theirreference values. The Traditional PI controller is used for speed control.

A. Generation of the Voltage Space Vector

Both the stator flux and electromagnetic torque arecontrolled directly by applying voltage switchingvectors of the inverter.The objective is to select theswitching vector voltagewhich gives the fastestresponse of the electromagnetic torque [12]. This selection process is based on hysteresis control of the torque and stator magnetic flux.

Equations (7) and (8) show that the stator magnetic flux and voltage space vector are in the same direction. Therefore, amplitude and direction control of the stator magnetic flux is possible by selecting suitable voltage space vectors. Voltage vector plane is divided into six parts as shown in Fig.3.Two adjacent vectors that yield the lowest switching frequency are selected in order to increase or decrease thestator fluxamplitude, respectively.

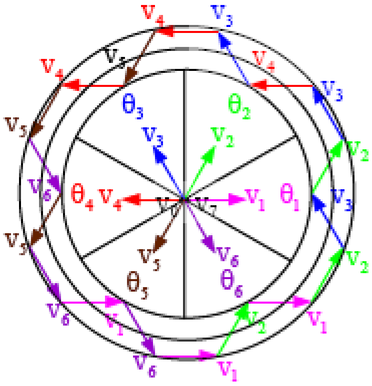

Fig.3. Vectors of space vector.

Table I. Switching vectors

Sectors		θ_1	θ_2	θ_3	θ_4	θ_5	θ_6
Sf=1	Sc=1	V_2	V_3	V_4	V_5	V_6	V_1
	Sc=0	V_7	V_0	V_7	V_0	V_7	V_0
	Sc=-1	V_6	V_1	V_2	V_3	V_4	V_5
Sf=0	Sc=1	V_3	V_4	V_5	V_6	V_1	V_2
	Sc=0	V_0	V_7	V_0	V_7	V_0	V_7
	Sc=-1	V_5	V_6	V_1	V_2	V_3	V_4

According to the figure, the flux regulator must ensure the flux evolution direction $\underline{\varphi_s}$ in order to maintain the error $\underline{\Delta\varphi_s}$ in the crown surface, and consequently the selection of the corresponding voltage vector.To maintain$|\varphi_s^* - \varphi_s| \leq \Delta\varphi_s$, we use a Hysteresis relay with two logic levels (output Sf = 1 and Sf = 0), this is the flux control law.

Table I shows the suggested switching sequences. For these different states, the hysteresis controllers can be used at the same timeas flux and torque hysteresis controllers.

B. Determining the Stator Flux Space Vector's Sector

The sectors (θ) can be determined using the equation:

$$\hat{\theta} = arct\,\frac{\hat{\varphi}_{\beta s}}{\hat{\varphi}_{\alpha s}} \qquad (12)$$

C. Determining the reference electromagnetic torque

According to equations (4) and (5) the reference torque value can beissuedfrom the PI controller which uses speed reference value as input. Within the torque hysteresis controller, the speed control output is limited by boththe torque limits and supply DC voltage of the inverter.

The block diagram of the proposed control scheme is shownin Fig. 4. The inverter is operatedbased on the different IGBT states given in Table I.

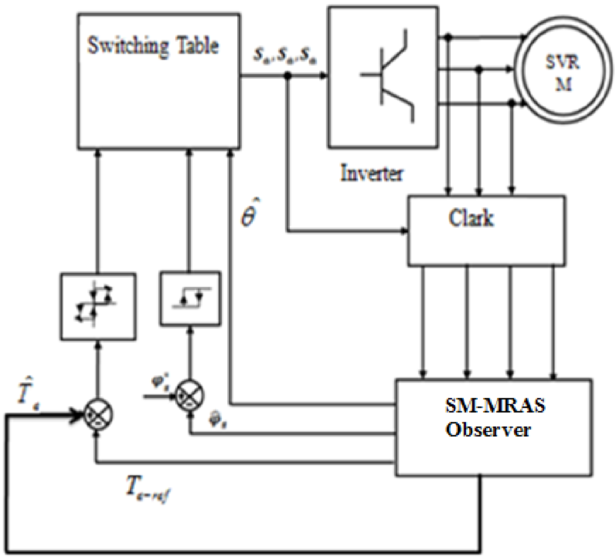

Fig.4. Block diagram of the proposed control scheme

IV. MRAS Observer

The proposed observer uses two models, the first onerepresents the reference model based onstator system equation (15) and the second represents the adjustable model expressedby equations (3). Fig .5 shows the block diagram of the proposed MRAS.

Reference model:

$$\begin{cases} \dfrac{di_{ds}}{dt} = -\dfrac{R_s}{L_d} i_{ds} + e_{qs} + \dfrac{1}{L_d} V_{ds} \\ \dfrac{di_{qs}}{dt} = -\dfrac{R_s}{L_q} i_{qs} + e_{ds} + \dfrac{1}{L_q} V_{qs} \end{cases}$$

(13)

Where e_{dqs} is thecompensating electromotive force that it is proportional to the stator current:

$$e_{dqs} = ki_{dqs} \qquad (14)$$

Equation (13) therefore becomes:

$$\begin{cases} \dfrac{di_{ds}}{dt} = -\dfrac{R_s}{L_d} i_{ds} + ki_{qs} + \dfrac{1}{L_d} V_{ds} \\ \dfrac{di_{qs}}{dt} = -\dfrac{R_s}{L_q} i_{qs} + ki_{ds} + \dfrac{1}{L_q} V_{qs} \end{cases}$$

(15)

The adjustable model is:

$$\begin{cases} \dfrac{di_{ds}}{dt} = -\dfrac{R_s}{L_d} i_{ds} + \omega \dfrac{L_q}{L_d} i_{qs} + \dfrac{1}{L_d} V_{ds} \\ \dfrac{di_{qs}}{dt} = -\dfrac{R_s}{L_q} i_{qs} - \omega \dfrac{L_d}{L_q} i_{ds} + \dfrac{1}{L_q} V_{qs} \end{cases}$$

(16)

The model (16) can be written in an estimated formas:

$$\begin{cases} \dfrac{d\hat{i}_{ds}}{dt} = -\dfrac{R_s}{L_d} \hat{i}_{ds} + \hat{\omega} \dfrac{L_q}{L_d} \hat{i}_{qs} + \dfrac{1}{L_d} V_{ds} \\ \dfrac{d\hat{i}_{qs}}{dt} = -\dfrac{R_s}{L_q} \hat{i}_{qs} - \hat{\omega} \dfrac{L_d}{L_q} \hat{i}_{ds} + \dfrac{1}{L_q} V_{qs} \end{cases}$$

(17)

We define the error dynamics:

$$\dot{\varepsilon} = \frac{d}{dt}\begin{bmatrix} \varepsilon_{\alpha s} \\ \varepsilon_{\beta s} \end{bmatrix} = \frac{d}{dt}\begin{bmatrix} i_{ds} - \hat{i}_{ds} \\ i_{qs} - \hat{i}_{qs} \end{bmatrix}$$

(18)

Let us make now the subtraction between (15) and (16), we obtain:

$$\frac{d}{dt}\begin{bmatrix} \varepsilon_{ds} \\ \varepsilon_{qs} \end{bmatrix} = \begin{cases} \dfrac{-R_s}{L_d} \varepsilon_{ds} + \omega \dfrac{L_q}{L_d} \varepsilon_{qs} + (\omega - \hat{\omega}) \dfrac{L_q}{L_d} \hat{i}_{qs} \\ \dfrac{-R_s}{L_q} \varepsilon_{qs} - \omega \dfrac{L_d}{L_q} \varepsilon_{ds} - (\omega - \hat{\omega}) \dfrac{L_d}{L_q} \hat{i}_{ds} \end{cases} \quad (19$$

)

We can write thesystem(19) in the following form:

$$\dot{\varepsilon} = A\varepsilon + B$$

(20)

Where $A = \begin{bmatrix} \dfrac{-R_s}{L_d} & \omega \dfrac{L_q}{L_d} \\ -\omega \dfrac{L_d}{L_q} & \dfrac{-R_s}{L_q} \end{bmatrix}$;

$$B = \begin{bmatrix} 0 & \Delta\omega \dfrac{L_q}{L_d} \hat{i}_{qs} \\ -\Delta\omega \dfrac{L_d}{L_q} \hat{i}_{ds} & 0 \end{bmatrix}$$

It is necessary to ensure the convergence of the estimation error towards zero, so that the system (20) would be stable. The stability of this algorithm is studied using the hyper-stability Lyapunov criterion [14].

We define the following Lyapunov function:

$$V = \varepsilon^T \varepsilon + \frac{\Delta\omega^2}{2\lambda} \geq 0 \qquad (21)$$

λ is a positive constant.

The function given by (21) is globally positivedefinite. Thus, $\dot{V} < 0 \quad \forall\ \hat{\omega}$

The time derivative of equation (21)is given by:

$$\dot{V} = \frac{1}{2}\left(\dot{\varepsilon}^T \varepsilon + \varepsilon^T \dot{\varepsilon}\right) + \frac{1}{\lambda} \Delta\omega \frac{d\Delta\omega}{dt} \qquad (22)$$

Let us replace $\dot{\varepsilon}$ by its value, we obtain:

$$\dot{V} = \frac{1}{2}\left(\varepsilon^T \left(A^T + A\right)\varepsilon\right) + \varepsilon^T B + \frac{1}{\lambda} \Delta\omega \frac{d\Delta\omega}{dt} \quad (23)$$

Where: $X = \frac{1}{2}\left(\varepsilon^T \left(A^T + A\right)\varepsilon\right)$

Wehave:

$$A^T + A = \begin{bmatrix} \frac{-R_s}{L_d} & -\omega\frac{L_d}{L_q} \\ \omega\frac{L_q}{L_d} & \frac{-R_s}{L_q} \end{bmatrix} + \begin{bmatrix} \frac{-R_s}{L_d} & \omega\frac{L_q}{L_d} \\ -\omega\frac{L_d}{L_q} & \frac{-R_s}{L_q} \end{bmatrix}$$

$$= -\begin{bmatrix} 2\frac{R_s}{L_d} & -\omega\left(\frac{L_q}{L_d} - \frac{L_d}{L_q}\right) \\ -\omega\left(\frac{L_q}{L_d} - \frac{L_d}{L_q}\right) & 2\frac{R_s}{L_q} \end{bmatrix} \langle 0$$

Then, the first term of (23) is negative.

For equation (23) to be negative, the second term must to be equal zero, i.e. $Y = 0$, then:

$$\frac{1}{\lambda}\Delta\omega\frac{d\Delta\omega}{dt} = -\varepsilon^T B \qquad (24)$$

Replacing by their expressions, we get:

$$\frac{1}{\lambda}\Delta\omega\frac{d\Delta\omega}{dt} = -\varepsilon^T B$$

$$\varepsilon^T B = \begin{pmatrix} \Delta\omega\frac{L_d}{L_q}\varepsilon_q & -\Delta\omega\frac{L_q}{L_d}\varepsilon_d \end{pmatrix} \begin{bmatrix} \hat{i}_{ds} \\ \hat{i}_{qs} \end{bmatrix}$$

$$= \Delta\omega\left(\frac{L_d}{L_q}\varepsilon_q\hat{i}_{ds} - \frac{L_q}{L_d}\varepsilon_d\hat{i}_{qs}\right)$$

Then:

$$\frac{d\hat{\omega}}{dt} = \lambda\left(\frac{L_d}{L_q}\varepsilon_q\hat{i}_{ds} - \frac{L_q}{L_d}\varepsilon_d\hat{i}_{qs}\right)$$

Finally the estimated speed is

$$\hat{\omega} = \lambda\int\left(\frac{L_d}{L_q}\varepsilon_q\hat{i}_{ds} - \frac{L_q}{L_d}\varepsilon_d\hat{i}_{qs}\right)dt \qquad (25)$$

To improve the precision amountswe should add a proportional gain to the integral action (K_p, K_i), then (25) becomes:

$$\hat{\omega} = K_p\left(\frac{L_d}{L_q}\varepsilon_q\hat{i}_{ds} - \frac{L_q}{L_d}\varepsilon_d\hat{i}_{qs}\right) + K_i\int\left(\frac{L_d}{L_q}\varepsilon_q\hat{i}_{ds} - \frac{L_q}{L_d}\varepsilon_d\hat{i}_{qs}\right)dt \qquad (26)$$

Or according to stator fluxes

$$\hat{\omega} = \frac{K_p}{L_q L_d}\left(\varepsilon_{q\varphi}\hat{\varphi}_{ds} - \varepsilon_{d\varphi}\hat{\varphi}_{qs}\right) + \frac{K_i}{L_q L_d}\int\left(\varepsilon_{q\varphi}\hat{\varphi}_{ds} - \varepsilon_{d\varphi}\hat{\varphi}_{qs}\right)dt \qquad (27)$$

Where: $\varepsilon_{d\varphi} = \varphi_d - \hat{\varphi}_d$ and $\varepsilon_{q\varphi} = \varphi_q - \hat{\varphi}_q$

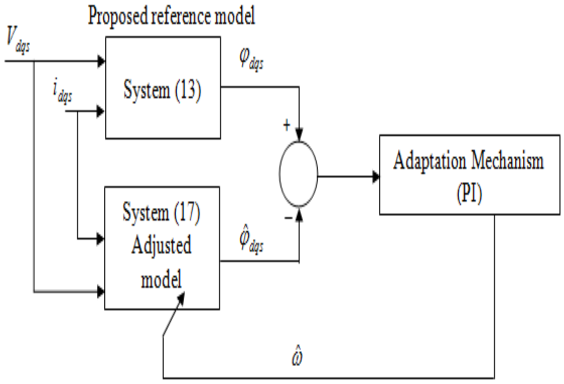

Fig.5. Block diagram of theMRAS observer.

V. Computer simulation results

Simulations were performed for both methods DTC and MRAS in the MATLAB/Simulink environment. The SynVRM parameters which are used in this simulation, are: $R_s = 0.9\Omega$; $L_d = 0.0127\ H$; $L_q = 0.0032H$; $J = 0.038\ Kg.m^2$; $f = 0.00013Nm.s/rad$; $p = 2$.

The performance of the sensorless control based on MRAS has beenverifiedwithawide range of speeds.Fig. 6-a shows that the motor starts without load, then the load is applied within the intervals [1.5s, 2.5s] and [5.5s, 6s].Moreover, estimated rotor speed error (Fig.6-b) is acceptable, so we can say that the proposedMRAS observerworks normally and stably.

Fig. 7 shows the waveform of the three-phase stator currents, they areindeed sinusoidal and the phase shift angle is 120^0.

Fig.8 shows thedirect and quadratic stator flux ($\hat{\varphi}_{\alpha s}$, $\hat{\varphi}_{\beta s}$), they are indeed sinusoidal. We notice that theload application has practically no effect on the stator flux evolution.

Fig.9 .Shows $\hat{\varphi}_{ds}$ and $\hat{\varphi}_{qs}$ .To be noticed thatfirst oneit correctlysettles and the second one follows the same shape as that of the torque.

The estimated electromagnetic torque is given byFig.10 is stable and it can be seen that boththe estimated $\hat{T}_e$ and real torque T_e correctly follow the torque reference.

Fig.11 shows the trajectory of the stator flux.With the estimation strategy based on MRASthe flux follows the command in an optimum way.

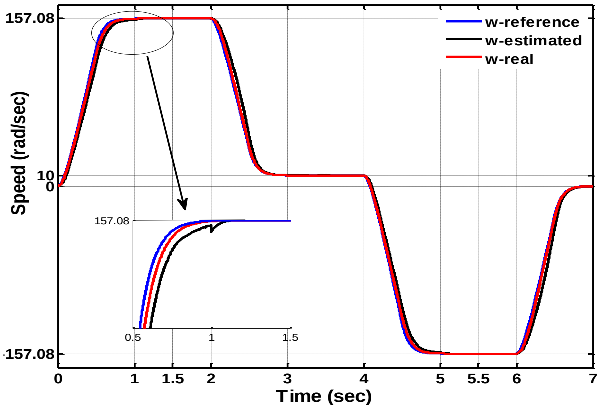

Fig.6-a.Reference, real and estimated speed

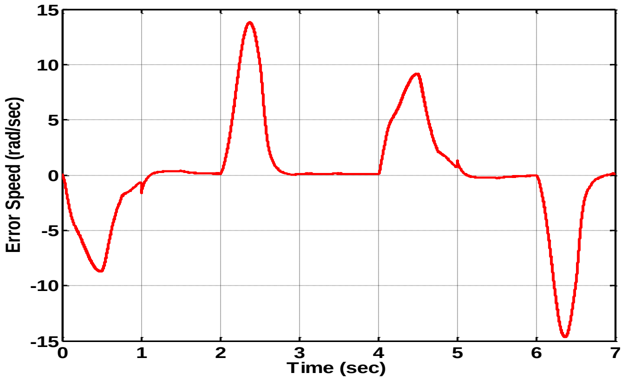

Fig.6-b.Error speed.

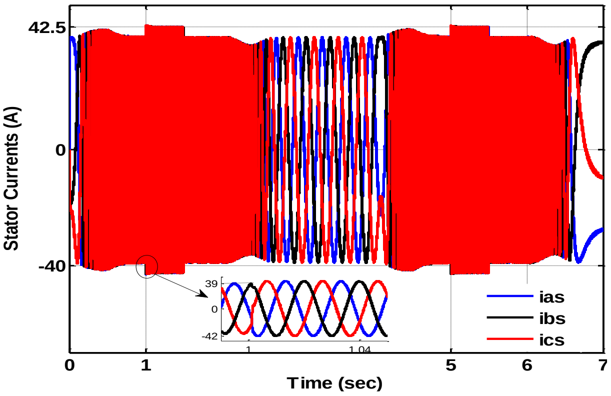

Fig.7. Stator Currents (i_{as} , i_{bs} , i_{cs}).

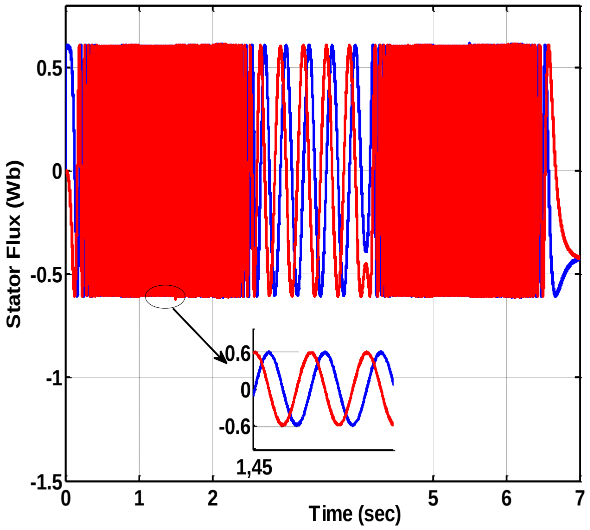

Fig.8. Stator Flux ($\hat{\varphi}_{\alpha s}$ and $\hat{\varphi}_{\beta s}$),

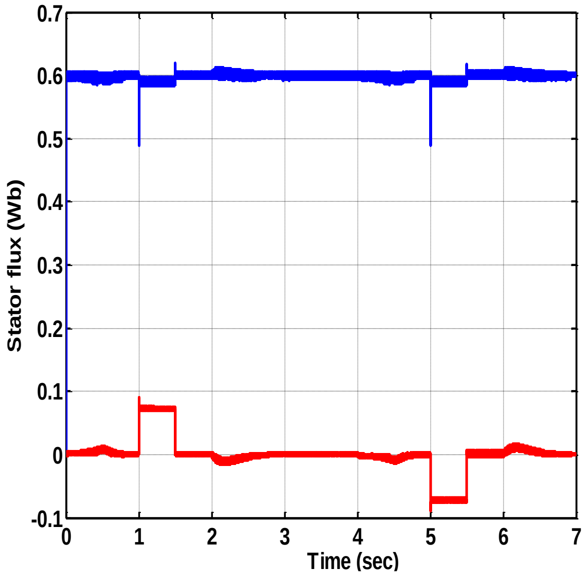

Fig.9. Stator direct and quadratic Flux ($\hat{\varphi}_{ds}$ and $\hat{\varphi}_{qs}$)

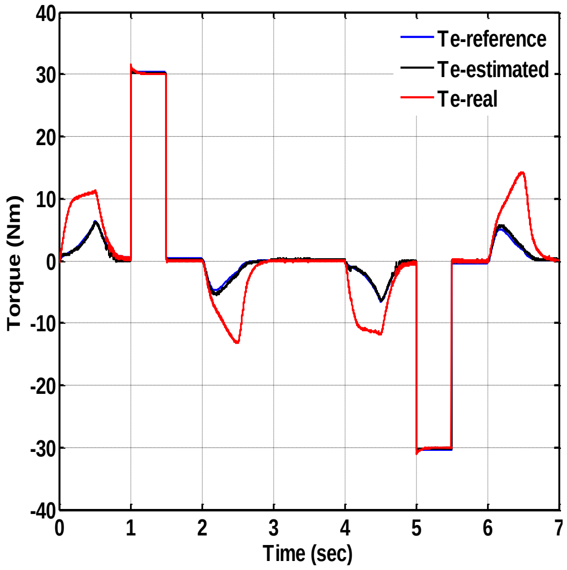

Fig.10. Electromagnetic Torque (T_e, $\hat{T}_e$ and T_{e-ref}).

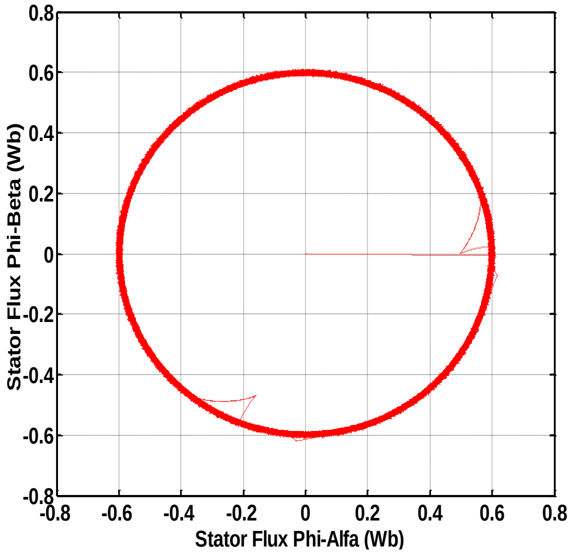

Fig.11.Stator Flux vector trajectory

VI. Conclusion

In this paper, a sensorless control of SynVRM drive based on DTC and MRAS observeris proposed. The DTC control technique works well in conjunction with the proposed observer. Good results have been obtained with respect to speed estimation. The estimation torque by DTC seems to be stable compared to that of induction motor.

Reference

[1] J. M. Park, S. Kim, J. P. Hong, and J. H. Lee, "Rotor design ontorque ripple reduction for a synchronous reluctance motor withconcentrated winding using response surface methodology", *IEEETrans. Magnet.*, vol. 42, no. 10, 2006, pp. 3479-3481.

[2] Jing-Can Li; Mao Xin; Zhen-Nan Fan and Renliu, "Design and Experimental Evaluation of a 12 k

W Large Synchronous Reluctance Motor and Control System for Elevator Traction", *IEEE* Access, Vol.8, February 27, 2020, pp. 34256-34264,DOI *10.1109/ACCESS.2020.2974414*

[3] AnantaramVaratharajan , Paolo PescettoGianmario Pellegrino, " Sensorless Synchronous Reluctance Motor Drives: A Full-Speed Scheme using Finite-Control-Set MPC in a Projection Vector Framework", *IEEETransactions on Industry Applications*, DOI 10.1109/TIA.2020.2990834,

[4]Tian-Hua Liu, Hsiao-Hao Hsu, "Adaptive Controller Design for a SynchronousReluctance Motor with Direct Torque Control",EUROCON 2007 The International Conference on Computer as a ToolWarsaw, September 9-12.

[5] Tian-Hua Liu, Hade SaputraHaslim, Shao-Kai Tseng, "Predictive Speed-loop Controller Design for aSynchronous Reluctance Drive System", 2016 International symposium on fundamentals of electrical engineering, University politechnicaof Bucharest, Romania, June 30 July 2, 2016.

[6] PradyumnaRanjanGhosh, Anandarup Das, G.Bhuvaneswari, "Performance Comparison of Different VectorControl Approaches for a Synchronous ReluctanceMotor Drive", 978-1-5090-4874-8/17/$31.00 ©2017 IEEE

[7] BehnamNikmaram, Jose Rodriguez, Cristian Garcia, "Simplified Modulated Model Predictive Control ofSynchronous Reluctance Motor" 978-1-7281-5849-5/20/$31.00 ©2020 IEEE.

[8]T. Matsuo and T. A. Lipo, "Rotor position detection scheme for synchronous reluctance motor based on current measurements," *IEEE Trans. Ind. Applicat.*, vol. 31, pp. 860–868, July/Aug. 1995.

[9] Wei-Lung Mao, Chao-Ting Chu ,Chung-Wen Hung," Synchronous Reluctance Motor Speed Tracking Using a Modified Second-Order Sliding Mode Control Method ",Neural Processing Letters (2020) 51:251–270 ,doi.org/10.1007/s11063-019-10085-x.

[10] ZbynekMynar, PavelVaclavek, PetrBlaha,”Synchronous Reluctance Motor Parameter and State Estimation Using Extended Kalman Filter and Current Derivative Measurement”, IEEE transactions on industrial electronics, vol. 68, No. 3, MARCH 2021

[11] Nur BEKIROGLU, Selin OZCIRA,“ Observer less Scheme for Sensorless Speed Control of PMSM Using Direct Torque Control Method with LP Filter*,” Advances in Electrical and Computer Engineering*, Volume 10, Number 3, 2010.

[12] Hailong Wu, Daniel Depernet, Vincent Lanfranchi, “ Analysis of torque ripple reduction in a segmented-rotorsynchronous reluctance machine by optimal currents,”Mathematics and Computers in Simulation 158 (2019) 130–147.

[13] C. M. Hackl, M. J. Kamper, J. Kullick, and J. Mitchell, “Current control ofreluctance synchronous machines with online adjustment of the controllerparameters,” in *Proc. IEEE 25th Int. Symp. Ind. Electron.*, Jun. 2016,pp. 153–160.

[17] B. Yassine, Z. Fatiha and L. Chrifi-Alaoui, “IS-MRAS With On-Line Adaptation Parameters Based onType-2 Fuzzy LOGIC for Sensorless Control of IM’’**,** Iranian Journal of Electrical and Electronic Engineering, inpress.ISSN: 1735-2827. 2020

(JMECS) J. Math. Eng. Comp. Sc.
Vol. 00, No. 00, pp. 11-18, (July 2024-Safar 1445$_H$)

Improving the performance of pin solar cell by optimizing its active layer

Saidi Mellal[a], Nahla Djebari[b] and Toufik Ziar[c]

[a]Larbi Ben M'hidi University of Oum El Bouaghi, Algeria
E-mail:.mellalsaida95@gmail.com

[b] Abbas Laghrour University of Khenchela,40000, Algeria
E-mail: Ndjebari@gmail.com

c Larbi Tebessi University of Tébessa, 12000, Algeria
E-mail: toufik1_ziar@yahoo.fr

Abstract. Efficiency of solar cell depends on absorbed photons and electron-hole pairs (carriers) generated in space charge region, the thickness of which has to be well chosen since the photocurrent is essentially due to the photogeneration of carriers in this region. It is therefore wise to artificially increase thickness of the space charge region by interposing an intrinsic layer I between the regions P and N, to obtain a PIN solar cell. In hydrogenated amorphous silicon (a-Si:H) PIN solar cell, a thick absorber layer (i-layer) can absorb more light to generate carriers, however, a thicker i-layer degrades drift electric field for carrier transport. On the other hand, a thin i-layer cannot absorb enough light. Thickness of i-layer is a key parameter that can limit the performance of amorphous thin film solar cells. In this context, we sought to improve the performance of PIN solar cell by optimizing the i-layer thickness. for this purpose, we have used Matlab software to carry out our simulations. Maximum efficiency of the cell is obtained at the 1.1 µm of thickness of i-layer.

Keywords. Solarcell, PIN structure, conversion efficiency, optimization, simulation.

AMS Classification:

I. Introduction

Generally, the single junction a-Si:H cell uses p-type layers of a-SiC:H semiconductor deposited on n-type a-Si:H semiconductor, with an intermediate intrinsic layer between p- and n-type layers. In this research, intrinsic a-Si:H layer is used, the choice of this material is justified by its low defect density, which gives to charge carriers in the depletion region a relatively long lifetime [1]. Also a-Si:H is a good absorber of light (absorption coefficient >10^5cm^{-1}),. However, the light-induced degradation of a-Si:H reduces the lifetime of carriers and the electric field in intrinsic layer degrades efficiency of the a-Si:H solar cell [2].

In order to improve the stability of solar cells, one way is to reduce the thickness of intrinsic layer to increase the electric field in that layer, which makes the solar cell less sensitive to light. However, when intrinsic layer is too thin, solar cell efficiency is limited by the amount of absorbed light . A good compromise is needed to improve performance of the PIN solar cell.

In order to find the optimal thickness and effectiveness by numerical simulation, we very the thickness of i-layer in ranges from 0.1 to 5 µm.

I. PHYSICS OF PIN STRUCTURE SOLAR CELL

The PIN silicon solar cell structure is shown in figure 1. It has an intrinsic layer which differs it from standard p-n solar cell. The existing layer is undoped and located between p-layer which is the emitter and n-layer which is the base. Addition of i-layer is needed because amorphous silicon solar cell has narrower depletion region area than crystalline. The three layers present in the PIN solar cell are very thin extrinsic layers and thicker intrinsic layer

[3]. The optical generation is also represented by phototransport mechanism.

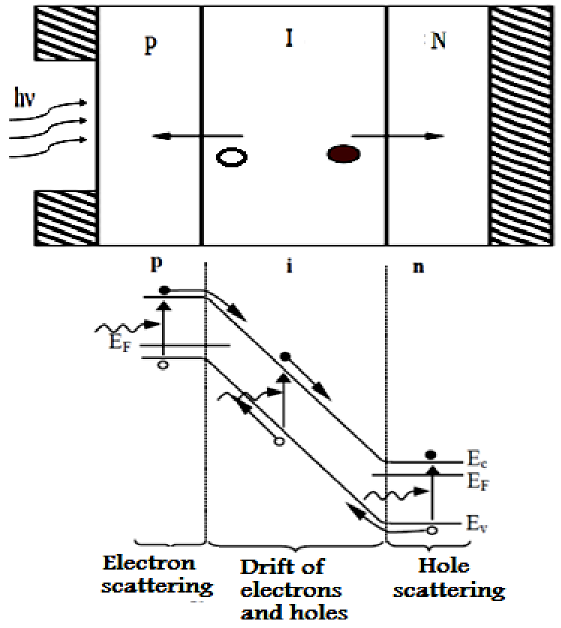

Fig.1.Schematic view and phototransport mechanism of PIN solar cell.

II. Modeling the photocurrent of charge carrier generation

The J_{Ph} photocurrent of solar cell defines the amount of electron-hole pairs created crossing the junction without recombination,it results from the sum of three components:

- The diffusion current of photoelectrons inp-layer.
- The photogeneration current in intrinsic layer.
- The diffusion current of phototholes of the n-layer.

The photocurrent calculation is obtained by summing all of these components at x = x_n (Fig. 2).

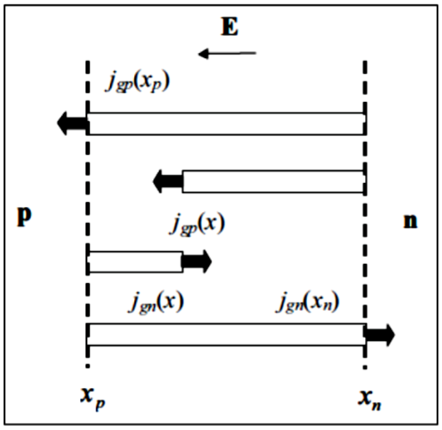

Fig.2. Currents in a PIN cell

Illumination of the solar cell with a photon flux Φ of energy greater than the band-gap width causes absorption of photons and generation of additional electron–hole pairs. As a result of the generation, an increase in the concentration of the excess electrons and holes in the three layers present in the PIN solar cell takes place. Since the absorption coefficient is α, the rate of the electron–hole pairs generation as a function of the depth from the surface of the illuminated p-layer can be expressed by the following formula[4]:

$$g(x) = \Phi\alpha e^{-\alpha x} \qquad (1)$$

A. Scattering current of electrons in p-layer

In p-layer, the electrons created (minority) diffuse towards the i-layer. By neglecting the electric field in this area,minority carrier diffusion is writtenas[5]:

$$\frac{d^2\Delta n}{dx^2} - \frac{\Delta n}{L_n^2} = -\frac{\Phi\alpha\tau_n}{L_n^2}e^{-\alpha x} \qquad (2)$$

With Δn the excess electrons in the p-layer, L_n the diffusion length of electrons and τ_n their lifetime.

Assuming that all electrons having reached the i-layer are propelled to the right by the electric field E, and the surface recombination at x = 0 is s_0, we obtain as boundary conditions for expression “(2)”:

$$\Delta n(x = x_p) = 0 \text{ and} s_0\Delta n(x = 0) = D_n\frac{d\Delta n}{dx}\bigg|_{x=0} \qquad (3)$$

We obtain the expression for Δn, by using the integration constants A_n and B_n calculated with the boundary conditions“(3)”:

$$\Delta n = A_n e^{(-x/L_n)} + B_n e^{(x/L_n)} + \frac{\Phi\alpha\tau_n}{1-\alpha^2L_n^2}e^{-\alpha x} \qquad (4)$$

The current of electron scattering at x = x_p is expressed by:

$$J_{ndiff}(x_p) = qD_n \frac{d\Delta n}{dx}\Big|_{x_p} \quad (5)$$

$$J_{ndiff}(x_p) = qD_n \left[\frac{A_n}{L_n} e^{(-x_p/L_n)} + \frac{B_n}{L_n} e^{(x_p/L_n)} - \frac{\Phi \alpha \tau_n}{1-\alpha^2 L_n^2} e^{-\alpha x_p}\right] \quad (6)$$

By neglecting the recombination in i-layer, all the electrons arriving at x = x_p are found at x = x_n, thus leading to:

$$J_{ndiff}(X_n) = J_{ndiff}(X_p). \quad (7)$$

B. Scattering current of holes in n-layer

In n-layer, the holes created (minority) diffuse towards the intrinsic layer. By neglecting the electric field in this area, the continuity equation of the excess holes Δp is written[5]:

$$\frac{d^2\Delta p}{dx^2} - \frac{\Delta p}{L_p^2} = \frac{\alpha \tau_p}{L_p^2} e^{-\alpha x} \quad (8)$$

with L_p the holes diffusion length and τ_p their lifetime.

Holes reaching the i-layer are evacuated to the left, and it is considered that L (length of the structure) is sufficiently large compared to L_n and 1/α. The boundary conditions are therefore:

$$\Delta p(x = L \to \infty) = 0 \text{ } et \text{ } \Delta p(x = L) = 0 \quad (9)$$

By using these boundary conditions, one obtains:

$$\Delta p = \frac{\Phi \tau_p}{1-\alpha^2 L_p} e^{-\alpha x_n}\left(e^{(-\alpha(x-x_n))} - e^{-(x-x_n)/L_p}\right) \quad (10)$$

The hole diffusion current at x = x_n is expressed by:

$$J_{pdiff}(x_n) = -qD_p \frac{d\Delta p}{dx}\Big|_{x_n} = -q\,\Phi \frac{\alpha L_p}{1+\alpha L_p} e^{-\alpha x} \quad (11)$$

C. Generation current in i-layer

Neglecting recombination in the intrinsic zone, the steady state continuity equation for the electron generation current is written:

$$\frac{1}{q}\frac{dJ_{gn}}{dx} + g(x) = 0 \quad (12)$$

Integration of"(12)"leads to:

$$J_{gn}(x_n) - J_{gp}(x_p) = -q\int_{x_p}^{x_n} g(x)\,dx = -q\int_{x_p}^{x_n} \Phi \alpha e^{-\alpha x} dx \quad (13)$$

The electron generation current is created from x_p to x_n, so $J_{gp}(x_p)$ is zero. We obtain after integration:

$$J_{gn}(x_n) = -q\Phi\left(e^{-\alpha x_p} - e^{-\alpha x_n}\right) \quad (14)$$

We can similarly calculate the hole generation current, created from x_n to x_p. This current is zero at x = x_n and the total generation current at x = x_n is therefore equal to the electron generation current:

$$J_g(x_n) = J_{gn}(x_n) \quad (15)$$

D. Total photocurrent

Total photocurrent J_{ph} is the sum of the currents described by expressions"(6)","(11)" , "(14)" and "(15)". The p-layeris in practice thin so that the number of electron-hole pairs created in i-layeris large. In this case, we can neglect electron scattering current "(6)"and consider that $x_p \simeq 0$ and $x_n \simeq W_i$(width of the i-layer). We finally get:

$$J_{ph} = J_g(x_n) + J_{pdiff}(x_n) = -q\Phi\left(1 - \frac{1}{1+\alpha_p L_p} e^{-\alpha w_i}\right) \quad (16)$$

II. REAL MODEL OF THE PIN SOLAR CELL

The one-diode model is the most popular to represent asolar cell thanks to its simplicity and precision [6].In a PIN solar cell, the phenomenon of recombination represents significant losses; which cannot be properly modelled using the one diode model. Consideration of these losses leads to introduce an additional diode [7,8].The equivalent electrical circuit of the model is shown in figure 3.

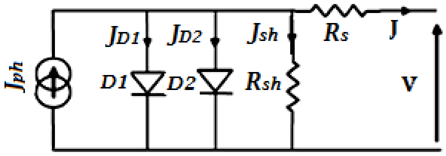

Fig. 3: Equivalent electrical circuit of solar cell, Two diode model

The output current is given by "(17)"[9].

$$J = J_{ph} - J_{s1}\left(\exp^{\frac{V+R_s.J}{n1\,.\,V_T}} - 1\right) - J_{s2}\left(\exp^{\frac{V+R_s.J}{n2.\,V_T}} - 1\right) - \frac{V}{F}.(17)$$

With: J_{ph}, Photocurrent of the cell; J_{s1} and J_{s2} are the reverse saturation currents of diode D1 and diode D2 respectively. The term containing J_{s2} in "(17)"compensates the loss by recombination in the space charge region as described in[10].

The factors n1 and n2 represent components of the diffusion and recombination current respectively. According to Shockley's diffusion theory, n1 should equal unity [10]. The value of n2 can vary. A better compatibility is obtained between the proposed model and the experiment if n2 ≥ 1,2.

The series resistance R_s is due to contribution of base and emitter resistances and contactsof front and rear faces. The shunt resistance$R_{sh}$is due to a leakage current at the junction.

$V_T = kT/q$ is the thermal voltage; k, Boltzmann constant; q, Electron charge; T, Cell temperature.

Reverse saturation currents are given by [11] :

$$J_{s1} = qn_i^2\left(\frac{Dpn}{L_{pn}N_D} + \frac{D_{np}}{L_{np}N_A}\right);\ (A.cm^{-2})(17)$$

$$J_{s2} = \frac{qW_i}{2}\cdot\frac{n_i}{\tau}(18)$$

With: *Wi*, the thickness of i-layer; *ni*, the intrinsic density ;τ, the lifetime.

III. Results and discussion

Throughout this work, the standard conditions for qualifying solar cells are used: AM1.5 and a temperature of 300 ° K. We start the simulation of a PIN solar cell shown in Fig.1. Then we go to optimize the parameter having a great influence on the efficiency of the cell in order to obtain the optimum performance there is. Theparameter in question is the thickness of the active layer .

A. *J (V) and P (V) characteristics*

Figure 4 and figure 5 express the J(V) and P(V) characteristics of a PIN solar cell. A lot of parameters relating to solar cell circuit could be extracted from this curves such as Jcc, *V*oc. Jcc represents the maximum density current at short circuit circumstance and reflects the capability of generating current. The open circuit voltage, *V*oc, is the maximum voltage available from a junction solar cell, and it occurs at zero currents. The *V*oc values were obtained from the intersection of the *I*-*V* curve and the horizontal axis voltages.

It is clear that the PINsolar cell offers a short circuit current of 31.55 mA/cm^2, an open circuit voltage of 0.74V, and a maximum power of 18.68mW / cm^2.

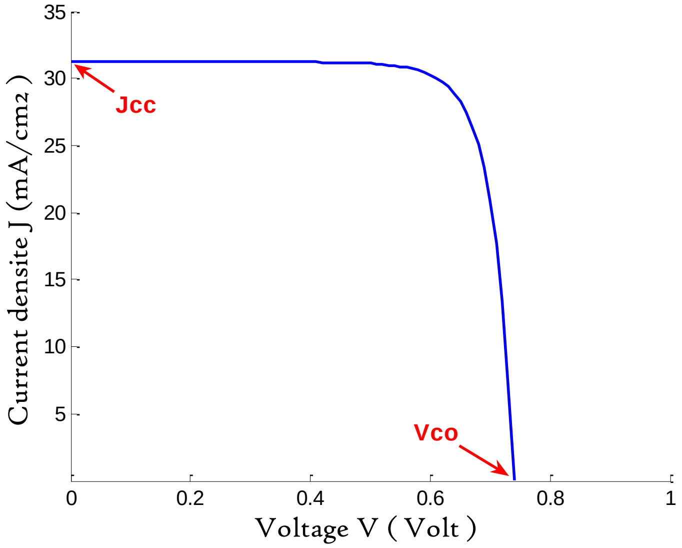

Fig. 4.Simulated current-voltage characteristic ofthe PINsollar cell.

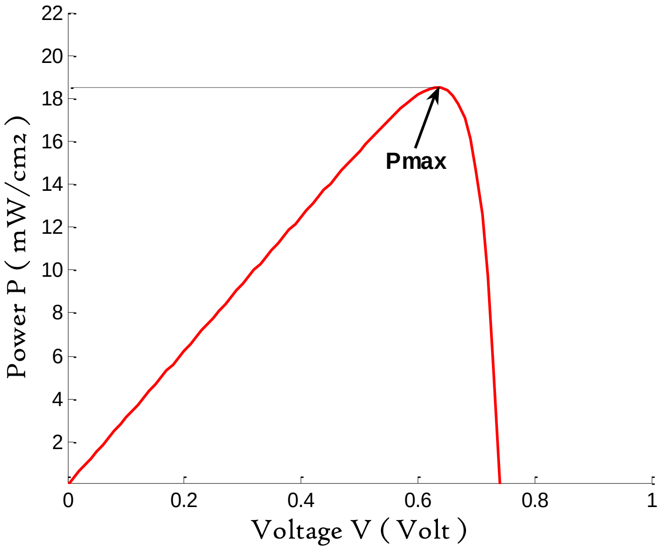

Fig.5. Simulated power-voltage characteristic ofPINsollar cell.

B. *Optimization of layer thickness*

We varied the thickness *Wi* (µm) of the intrinsic layer of our model in an interval ranging from 0.5 to 6 µm, then we noted the different parameters of PIN cell.

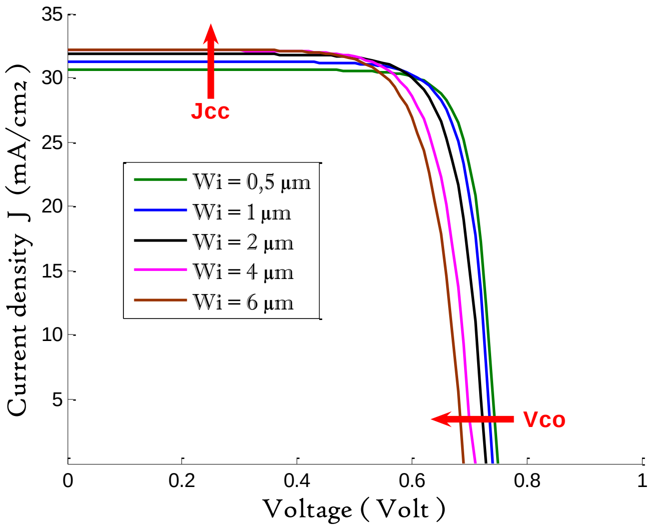

Fig.6. Current-voltage characteristics for different thicknesses of intrinsic layer

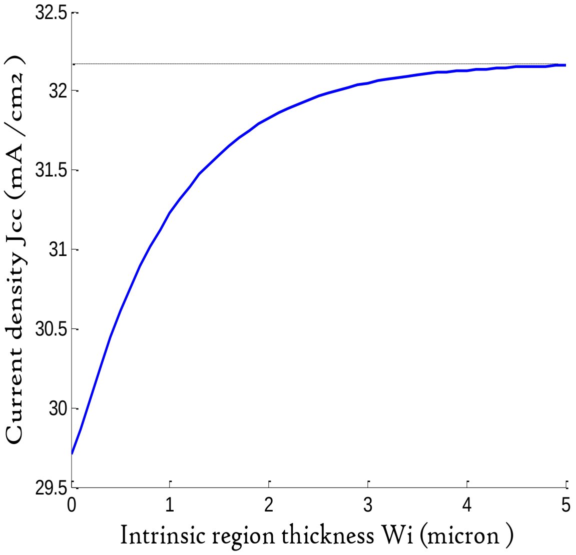

Fig. 7. Short-circuit current (Jcc) accordingintrinsic layer thickness

Figures 6 and 7, shows that the short circuit current *Jcc* increases with the increase of i-layer thickness *Wi*, it reaches 32.17 mA /cm^2. With an increase in i-layer thickness, the more photon energy will be absorbed and multiply the electron-hole pairs generation.On the contrary, the open circuit voltage decreases with the increase of i-layer thickness, since it depends on the geometry of the junction considered.

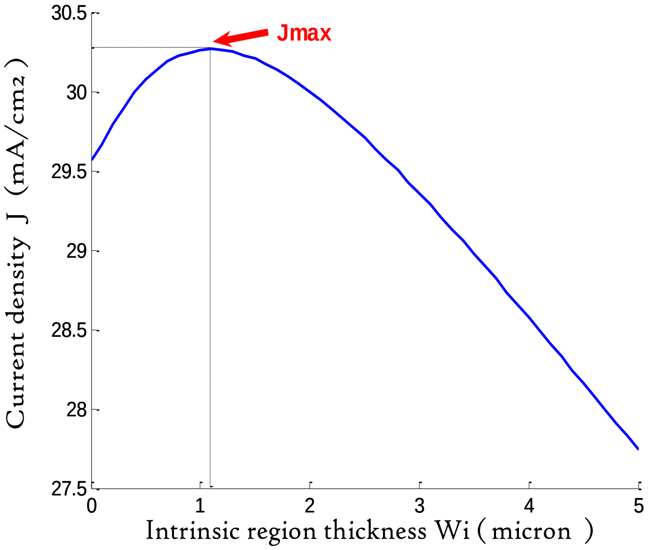

Fig. 8. Output current for different thicknesses of intrinsic layer

Figure 8 shows that as soon as an intrinsic layer of 0.5 µm is integrated, the current delivered by the cell increases. The intrinsic layer extends the space charge zone of the cell and therefore increases photons absorption and collection speed of the photocurrent, therefore the delivered photocurrent density increase up to a maximum value of 30, 27 mA /cm^2 for Wi ranging from 0.75 µm to 1.5 µm then decreases for values greater than this thickness, due to the fact that the increase in the thickness of the intrinsic zone increases the possibility of photo carriers recombination.

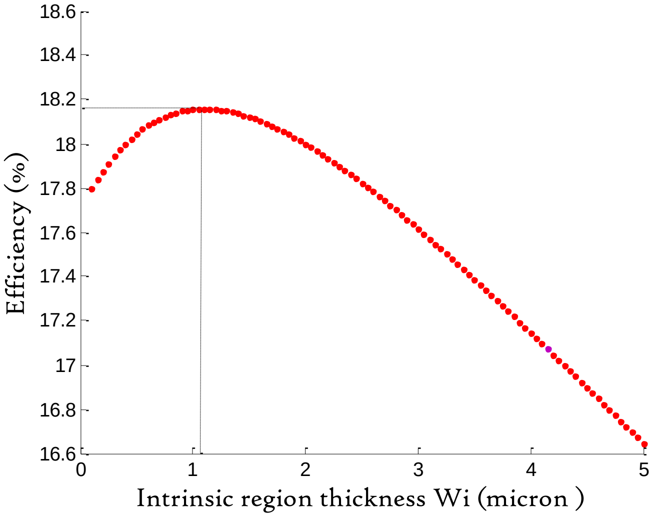

Fig.9. Cell efficiency according intrinsic layer thickness

Another key performance characteristic of a solar cell is the efficiency η, which is the ratio of maximum output power to the incident light power.

From figure 9, we notice that efficiency conversation varies with the thickness *Wi*. It reaches a maximum value of 18.16% for a thickness of *Wi* = 1.1µm. Above 1.1 µm the efficiency decreases. As thickness *Wi* increases, the electrons generated can recombine before reaching the contacts and so will not be collected, consequently the decrease in efficiency. From these key performance characteristic, we can understand that the optimized thickness of the i-layer is in the range around 0.75 to 1.5 μm. The quality of the i-layer is dependent also on the thickness.

IV. Conclusion

The numerical analysis of a-Si:H/a-SiC:H single-junction solar cell with i-layer used as the intermediate absorbing layer (a-Si:H) placed between layers of p-type (a-SiC:H) and n-type (a-Si:H) has been conducted. It is established that, after optimizing the solar cell parameters, its highest efficiency of 18.16% is achieved at 1.1µm thickness of i-layer. The maximum experimental value of the similar solar cell efficiency is 10.1% [12].

For a thinner thickness of the i-layer, the solar cells could not effectively absorb all of the sunlight. Therefore, the short circuit current and the output power would be low. In addition, many point defects are generated in the sample with a thicker layer and the recombination phenomena are greater, which weakens the photo-generated current.

The cell conversion efficiency can be much improved compared to a single PIN junction structure if two or more PIN structure diodes with preferably different optical gaps are stacked on top of each other.

The focus on manufacturing solar cells is not sufficient for the overall performance improvement. Another important aspect to study rigorously is the phenomenon of degradation induced by light observed in cells based on a-Si:H.

REFERENCES

[1] R.J. Koval, J.M. Pearce, A.S. Ferlauto, R.W. Collins, and C.R. Wronski, “Evolution of the Mobility Gap with Thickness in Hydrogen-Diluted Intrinsic Si:H Materials in the Phase Transition Region and Its Effect on p-i-n Solar Cell Characteristics,” The Center for Thin Film Devices, Pennsylvania State University, University Park, PA 16802, 2019.

[2] A. NAMODA, “ Dégradation (effetstaebler-'Wronski) et caractérisation des cellule solaires à base de silicium amorphe hydrogéné (a-Si:H),” M. doctorat. thesis, Metz University, France, June. 1999.

[3]

[4] I. Benigno, Darminto, “Effect of Intrinsic Layer Energy Gap and Thicknesses Optimization on the Efficiency of p-i-n Amorphous Silicon Solar Cell,” *IPTEK, Journal of Science, vol. 2, no. 3,* pp. 37–42, 2017.

[5] Suproniuk, M., Wierzbowski, M. &Paziewski, P. Effect of generation rate on transient photoconductivity of semi-insulating 4H-SiC. Sci Rep 10, 11865 (2020).

[6] G. Adolf, K. Joachim, V. Bernhard, “Crystalline Silicon Solar Cells“*Fraunhofer Institute for Solar Energy Systems*, Freiburg, Germany, 1998

[7] Y.-J. Wang and P.-C. Hsu, “An investigation on partial shading of PV modules with different connection configurations of PV cells,” *Energy, vol. 36, no. 5*, pp. 3069–3078, May 2011.

[8] J.A. Gow and C.D. Manning « Development of a Photovoltaic Array Model for Use in Power Electronics Simulation Studies ». *IEE Proceedings on Electric Power Applications, Vol. 146, N°2*, pp. 193 - 200, 1999.

[9] C-T Sah, R.N. Noyce and W. Shockley, “Carrier Generation and Recombination in Pn Junctions and Pn Junction Characteristics,” *Proc. IRE, vol. 45, n°9*, pp. 1228 - 1243, 1957.

[10] K. Ishaque, Z. Salam, H. Taheri, and Syafaruddin, “Modeling and simulation of photovoltaic (PV) system during partial shading based on a two-diode model,” *Simul. Model. Pract. Theory, vol. 19, no. 7*, pp. 1613–1626, Aug. 2011

[11] K. Kety , K.A. Amou , K. Sagna , K. Tepe, Y. Lare and K. Napo1, “Modélisation et simulation d’un générateur photovoltaïque: Cas du module polycristallinEcoline LX-260P installé au dispensaire de Sévagan (Togo),” *Renewable Energies Review*, vol. 19, pp. 633–645, 2016.

[12] A. Vauthelin, “Fabrication et caractérisation de cellules photovoltaïques multi-jonctions à base de matériaux antimoniures (III-Sb) pour applications sous fortes concentrations solaires,” M. doctorat. thesis, Montpellier University, France, Nov. 2018.

[13] I.M. Kabir, S.A. Shahahmadi, “Amorphous Silicon Single-Junction Thin-Film Solar Cell Exceeding 10% Efficiency by Design Optimization,” *International Journal of Photoenergy*, 2012.- Article ID 460919.-7pages.

(JMECS) J. Math. Eng. Comp. Sc.
Vol. 00, No. 00, pp. 19-32, (July 2024-Safar 1445$_H$)

Signals Denoising Using Fractional Wavelets

Lanani Abderrahim and Aboudi Abdelaziz

Abbas Laghrour University of Khenchela, Algeria.

E-Mail: lanani_arahim@yahoo.fr

Abstract. In order to illustrate the potential and efficiency of fractional wavelets compared to the different wavelets existing in the literature, one of the applications of wavelets is presented in this paper. This is the denoising of signals by thresholding fractional wavelet coefficients. Two fractional wavelet bases are used: fractional Haar wavelets and fractional wavelets with compact support. These wavelets have interesting characteristics and properties, where the flexibility of the associated filters and its high selectivity offer to these bases a great ability to support several digital signals processing in a very efficient manner. The experimental results obtained are satisfactory and promising; they show that the performance of fractional wavelets is superior to that of classical wavelets; this is due to the flexibility and high selectivity of fractional filters associated with these fractional bases.

Keywords. Denoising - thresholding - fractional filters - fractional wavelets

AMS Classification

I. Introduction

In recent decades, signal denoising has been the subject of much research. It has received a great deal of attention in the technical and scientific literature, and is still the subject of an extensive research. The aim is to estimate an unknown function g from its noisy measurements.

Several methods of denoising have been proposed and developed, very intuitive at the outset, but increasingly complex. Starting with conventional filtering methods [1], these involve using a low-pass filter to remove high frequencies, which has the disadvantage of attenuating all the details of the signal. In order to overcome these problems, new, more efficient techniques were developed during the 1990s, notably variational approaches based on EDPs [2], [3], approaches using Markov fields [4-6] and multi-scale transforms approaches, including wavelet transformation [7].

Recently, wavelets have shown their power in the context of statistical estimation [8], through these parsimonious transforms the energy of the useful signal is concentrated on a small number of coefficients, which provides a non-linear natural framework for estimating this signal. In fact, it is enough to threshold the coefficients of the observed signal and to invert the transform to obtain an estimate of the useful signal.

Moreover, among the wavelets which are currently of considerable interest those based on fractional calculus, the main advantage of having a fractional order is flexibility, which allows adjustments in transform parameters such as regularity and localization of the base functions [9]. These advantages can be exploited to improve several approaches and solve many problems in signal processing, condition-based maintenance of rotating machines, Incompressible fluid flows in Turbulence…

The aim of the present paper is to introduce a denoising algorithm based on fractional wavelets, begin with the general formalism of the denoising problem, and then we will see the principle of denoising by thresholding wavelet coefficients, of which we will describe the different steps necessary during the denoising process. Then, we will show the results of the application of fractional wavelets for signals denoising, these results will be compared with those obtained by the application of known classical wavelets such as Haar, Daubechies, Coiflettes, Symlettes, Meyer and the bi-orthogonal wavelets.

II. General formulation of the problem

The problem of denoising (known as “non-parametric regression” in mathematical statistics [8]) can be put in the following general form:

$$y_{mn} = g_{mn} + \varepsilon_{mn} \qquad (1)$$

Where our degraded observations $y_{m,n}$, $m,n=0,\ldots,N-1$ are modeled as the sum of a signal $g_{m,n}$ to be estimated and a Gaussian white noise ε_{mn} of zero mean and variance σ^2. By applying the DWT [7] on the noise signal we obtain the following Equation:

$$\begin{cases} c_{mn} = a_{mn} + \varepsilon_{mn} \\ d_{mn}^{oj} = s_{mn}^{oj} + \varepsilon_{mn} \end{cases} \quad (2)$$

With $m,n = 0,\ldots,2^{j_c} - 1$and $j = J_c,\ldots,J-1$.
Where $a_{m.n}$represents the DWT approximation coefficients of the signal g at the position *(m, n)*and s_{mn}^{oj} represents the DWT detail coefficients of signal g at position *(m, n)*, scale j and orientation o. Due to the orthogonal character of the wavelet transform, the ε_{mn} coefficients are independent random variables that also define a Gaussian white noise.

III. General principle of denoising by thresholding of wavelets coefficients

In general, it is possible to make a wavelet decomposition of a signal and then to reconstruct this signal from its wavelet coefficients. However, this technique would not be very useful if we did not modify these coefficients because we would obtain a final signal identical to the initial signal.
Wavelet coefficients mark the discontinuities that occur in the signal. So they match the details. If we now threshold these coefficients, it means eliminating the finer details of the signal. Two major applications of this technique of thresholding wavelet coefficients are therefore created: compression and denoising [10]. In fact, all conventional denoising approaches are approaches based on judicious selection of signal coefficients, coefficient by coefficient. Due to the hollow character of the multi-scale transforms (wavelets) [11], we can intuitively assume that only a few detail coefficients with a sufficiently high value contribute to the signal to be recovered g, whereas the coefficients of low values are essentially due to noise which uniformly contaminates all coefficients. It is also recommended to keep the approximation coefficients. These, related to low-frequency components, essentially characterize the original signal.
The following diagram shows the complete process of denoising in the domain of multi-scale transforms.

$$y \xrightarrow{\Phi^T} \left\{c_{mn}, d_{mn}^{oj}\right\} \xrightarrow{non-linear-estimator} \left\{c_{mn}, \delta_\lambda(d_{mn}^{oj})\right\} \xrightarrow{R} \hat{g}$$

Where Φ^T represents a multi-scale transform and R is the reconstruction operator.$\delta_\lambda$is a non-linear operator of type coefficients thresholding, based on the full conservation of coefficients $c_{m,n}$ and a careful selection of coefficients d_{mn}^{oj}. The coefficients having been processed, the restored signal is reconstructed by the inverse transform.

A. *stimation of noise level*

Donoho&Johnstone proposed an estimate of noise [12], using a classical result in robust statistics:

$$\hat{\sigma}_\varepsilon = \frac{MAD(\{d_{mn}^{J-1}\})}{0.6745} \qquad (3)$$

where MAD is the absolute median value of the detail coefficients of the finest scale. Factor 0.6745 is selected after calibration with a Gaussian distribution. This very robust estimator is also very popular for multi-scale denoising.

B. Thresholding

The functions of thresholding come in two forms, *hard*thresholding and *soft*thresholding [13-14].

In recent years, several methods have been proposed in order to find a compromise between hard and soft thresholding [15 - 18], such as: FIRM, NNG, SCAD thresholding and TNN thresholding [19], where each of these estimation functions is dependent on the choice of the λ threshold.

C. Choice of threshold

There are many methods to determine the threshold value, the most widely used are proposed by Donoho&Johnstone in [20 - 21] under the name of the *minimum threshold*, *universal threshold* and the famous *SureShrink*.

IV. Fractional wavelets

Fractional wavelets are generalizations of classic wavelets. They are proposed to rectify the limitations of fractional Fourier transform (FRFT). They have the ability to represent signals in the time/frequency domain, with more flexibility and precision.

In these last decades, fractional wavelets have been proposed with its two versions continuous and discrete,the idea of which is based initially on the combination of the classical wavelet transform with the fractional Fourier transform [22]. Quickly the idea is reformulated, where the construction becomes simpler, more precise and does not present a great difficulty, especially for the continuous case whose use of mathematical functions with the integration of the notions of fractional derivative, during the construction, facilitated the operation. We can cite by way of example the wavelets resulting from the Gaussian function and its fractionalderivatives, the spline function with fractional degrees [23] and the Cole-Cole distribution function [24]. However, in the discrete case, the definition of the discrete fractional wavelet transform is not yet reported in the literature. Therefore, a definition is consolidated by discretizing its continuous version. On the other hand, the construction of discrete fractional wavelet bases can be achieved with the generalization of the filters that constitute them, via the use of fractional digital delay [25] [26], where The construction generally begins with the choice of a low-pass digital filter with the orthogonality property checked in Fourier or direct space; then it is generalized through the fractional delay (FD) Z^{-D}, where the delay Z^{-n} will be replaced by a fractional delay Z^{-D} , $D \in \mathbb{R}$, while ensuring correct properties of orthogonality, compact support and regularity.

Furthermore, and because of its irrational function representation, the fractional digital delay will be simulated by a filter called the *fractional delay filter*[27]. It is then possible to construct by a simple modulation, the fractional filter passes high from the fractional filter passes low and deduce by the cascade algorithm [28] the associated scaling function and wavelet.

In this paper, we have based on two bases: *fractional Haar wavelets* and *fractional wavelets with compact support* [25-26]. These wavelets have interesting characteristics and properties, where the flexibility of the associated filters and its high selectivity offer to these bases a great ability to support several digital signal processing (windowing, debugging, compression, detection, filtering and reconstitution) in a very efficient manner.

V. Signals denoising by fractional wavelets

As part of a dyadic analysis, a SureShrink type threshold (Stein’s unbiased risk estimator) and a hard thresholding, we applied a denoising algorithm, based on fractional wavelets on a set of signals corresponds to those constructed and analyzed in [29]: Blocks, Bumps, Heavy-sine (see Figure 1). These are non-stationary signals such as medical signals (ECG, EEG, EMG, etc.) seismic signals and vibration signals from rotating machines...

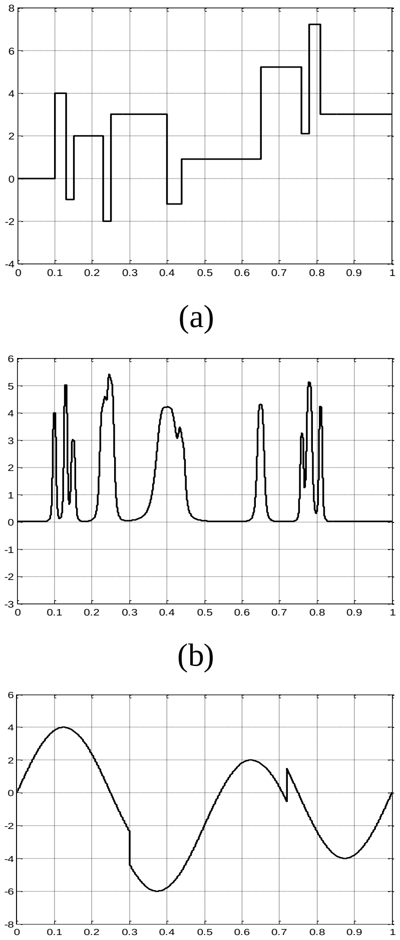

(a)

(b)

(c)

Figure.1 Test signals: (a) Signal 'blocks'; (b) Signal 'bumps'; (c) Signal 'Heavy sines'

Signals are corrupted by Gaussian white noise of standard deviation 10, 20 and 30 (Figure 2). We quantify the quality of the denoising by calculating the signal-to-noise-ratio (SNR) which is defined as follows:

$$SNR = 10 \cdot log_{10} \frac{P_{signal}}{P_{noise}} \qquad (4)$$

Where P_{signal}, P_{noise} represent respectively signal power and noise power.

VI. Experimental results

A. Results of Fractional Haar Wavelet Application

We apply the denoising algorithm based on fractional Haar wavelets for different values of the parameter *D* (adjustment parameter of the filters that constitute them) on the noisy signals: Blocks, Bumps and Heavy-sine, with standard deviations of 10, 20 and 30. Figure 3 shows the denoising results for *D=0.5... 1.5*, however Table 1 summarizes all the results obtained including the ordinary case (Haar classic where D=1). The results vary depending on the type of signal and the amount of noise (the value of the standard deviation). In the case of the Blocks signal we see that there is an improvement of the SNR but remains comparable to the results obtained by the use of the classic Haar wavelet especially for the case where σ =10, on the other hand, in the case where σ =30, we can see that there is a remarkable preference for fractional wavelets (*D=1...1.5*) over the classic case (*D=1*). On the other hand, in the case of Bumps and Heavy-sine signals, we see that the results obtained by the fractional wavelets are higher than that obtained by the classical Haar wavelets (*D=1*).

Figure 4 shows the variation of the SNR (calculated over 20 simulations) as a function of parameter *D*, for different standard deviations (sigma = 10, 20 and 30). It appears that the best value of the SNR for all signals corresponds to a fractional value of parameter D; this indicates that fractional analysis leads to an improvement of the denoising result,this due to the flexibility of fractional filters that make up the fractional wavelet bases.

B. esults of Application of fractional wavelets with compact support

In this section, we apply the denoising algorithm based on fractional wavelets with compact support on the set of noisy signals:

Blocks, Bumps and Heavy-sine. It should be noted that the lengths of the fractional delays (*m1*, *m2* and *m3*) which constitute the fractional wavelets with compact support are limited in the following intervals:

$m1 \in [0.1\,,0.7],\ m2 \in [0.1\,,1],\ m3 \in [0.2\,,1.7]$ [26].

Figure 5 shows the denoising results for different values of *m1*, *m2* and *m3*. On the other hand, we have grouped the best results obtained in Table 2, where it appears the good improvement of the signal to noise ratio (SNR). Figure 6 shows the variation of the SNR (calculated over 20 simulations) as a function of the parameters *m1*, *m2* and *m3*, for different standard deviations (sigma=10, 20 and 30). Note that the best value of the signal to noise ratio for all the signals always corresponds to a fractional value.

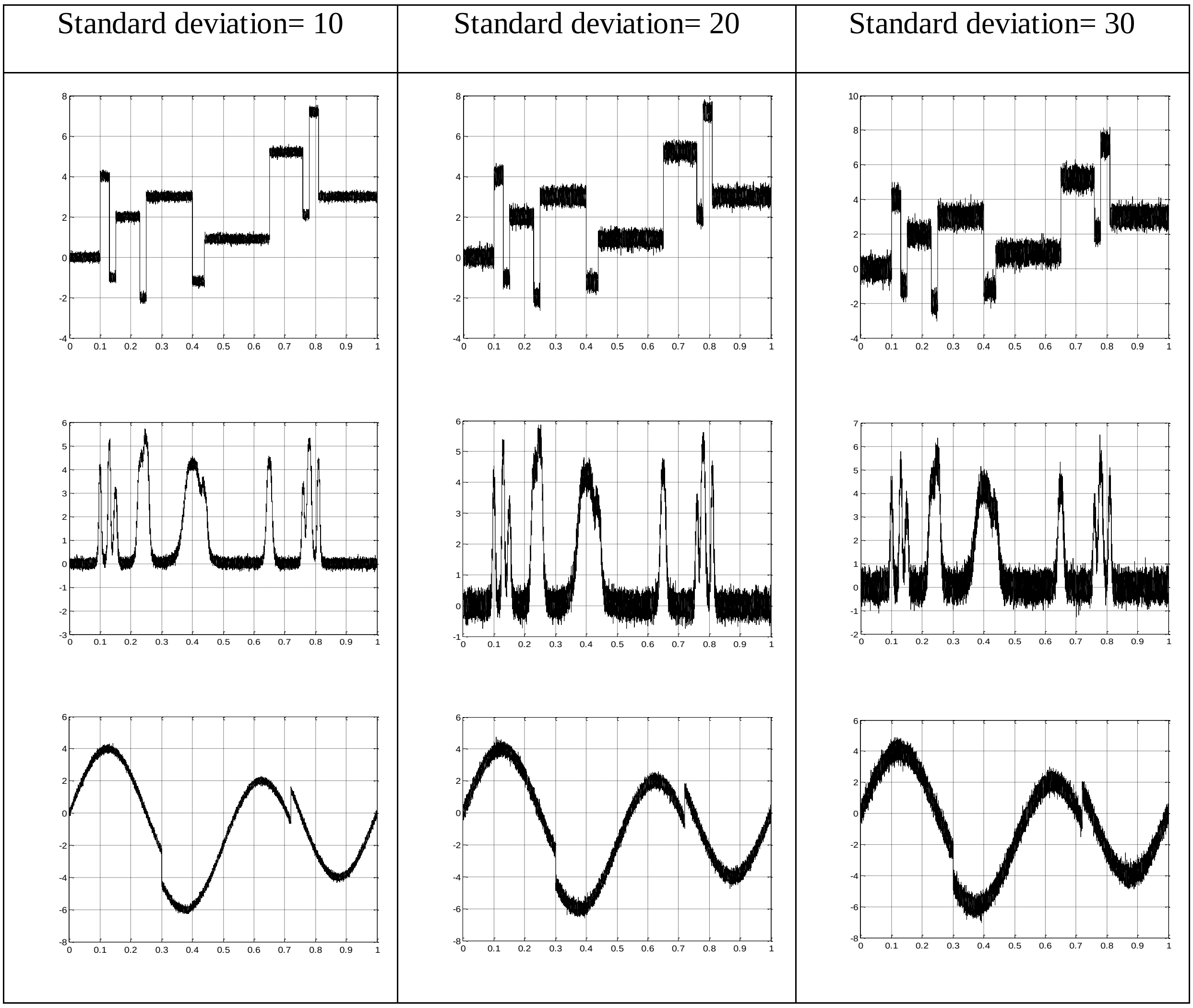

Figure.2 Noisy test signals with Gaussian white noise with standard deviation 10, 20 and 30.

Table 1 Signal denoising results: 'Blocks', 'Bumps' and 'Heavy sine' for different values of D. (Fractional Haar wavelet)

Input signals	*σ/SNR Noisy signals*		*SNR Denoised signal (dB)*								
		D=0.6	D=0.7	D=0.8	D=0.9	*Haar*	D=1.1	D=1.2	D=1.3	D=1.4	D=1.5

Blocks	σ =10 (29.45)	30.27	31.64	33.03	34.66	35.87	36.59	36.53	36.25	36.62	34.71
	σ =20 (23.46)	25.44	26.34	27.46	28.52	29.82	30.86	31.25	31.55	31.00	31.26
	σ =30 (19.92)	21.64	22.22	23.00	23.44	24.90	26.73	27.41	27.82	27.75	28.11
Bumps	σ =10 (25.11)	29.36	29.45	30.16	30.32	30.40	31.16	31.39	31.87	31.21	31.91
	σ =20 (19.09)	23.65	24.29	24.76	24.97	25.20	25.69	25.83	25.86	26.37	25.80
	σ =30 (15.55)	20.82	20.92	21.04	21.84	20.81	22.01	22.70	23.01	21.45	22.70
Heavy sine	σ =10 (29.87)	32.43	32.72	33.49	33.89	34.89	35.83	36.41	36.65	36.70	36.91
	σ =20 (23.76)	26.27	26.77	26.92	27.49	28.06	29.19	29.66	29.67	29.89	30.27
	σ =30 (20.26)	22.12	22.59	23.24	23.61	23.99	24.46	25.28	25.33	25.69	25.82

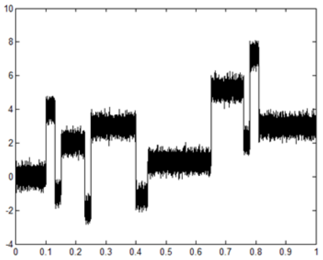
Noisy signal (Blocks 30%)

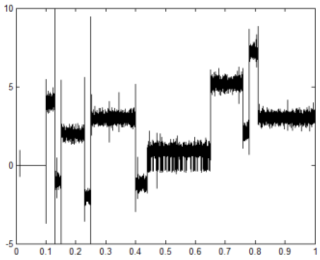
D = 0.5

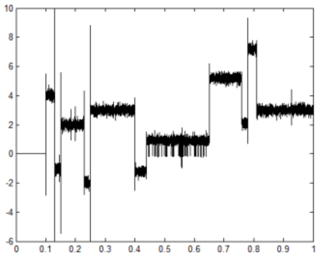
D = 0.8

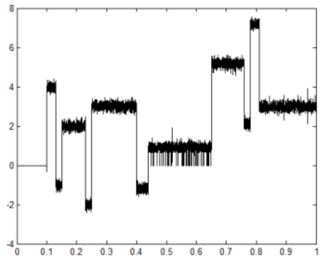
D = 1

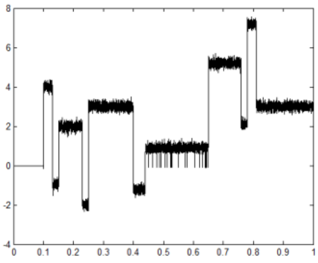
D = 1.3

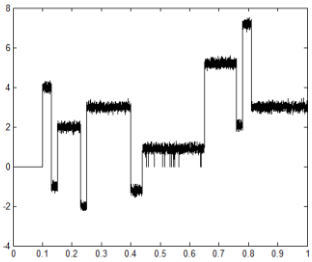
D = 1.5

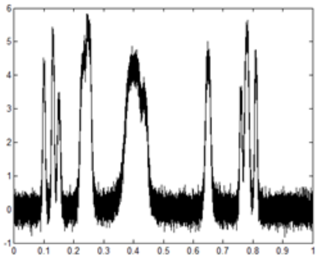
Noisy signal (Bumps 20%)

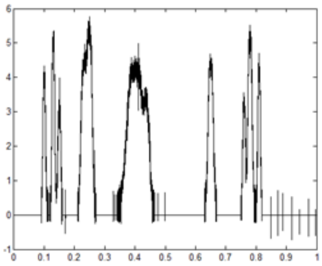
D = 0.5

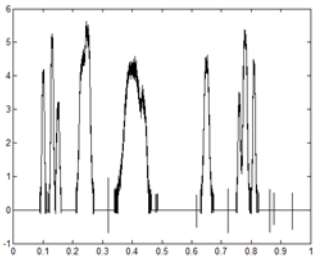
D = 0.8

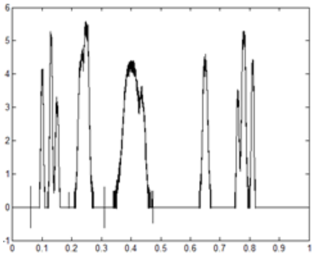
D = 1

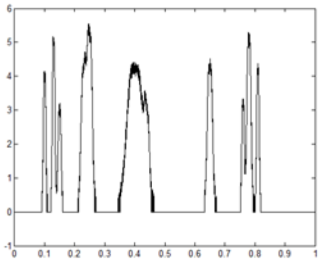
D = 1.3

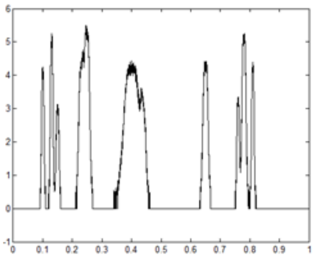
D = 1.5

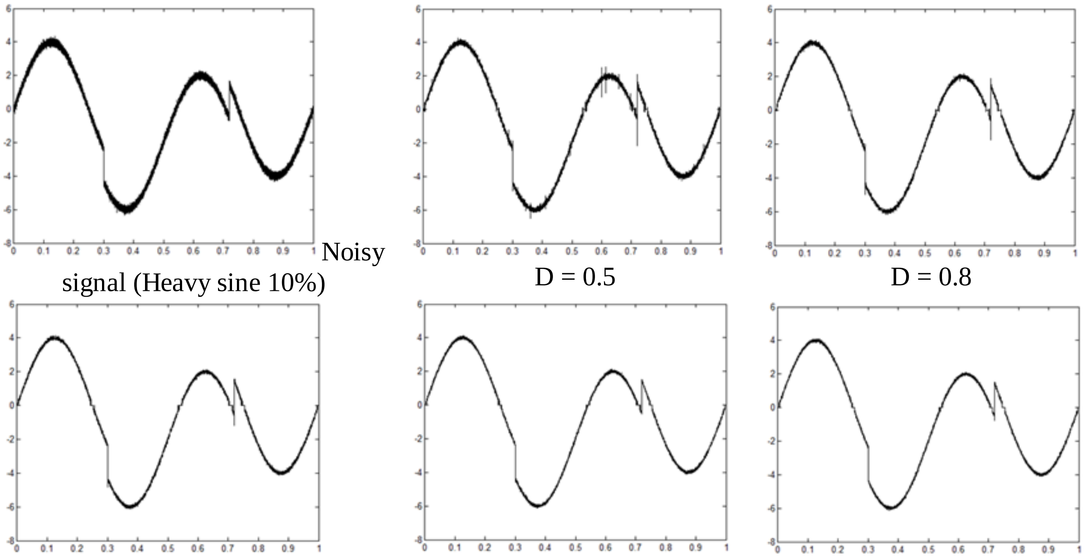

Noisy signal (Heavy sine 10%) D = 0.5 D = 0.8

D = 1 D = 1.3 D = 1.5

Figure.3 Visual results of denoised signals.
(Fractional Haar wavelet)

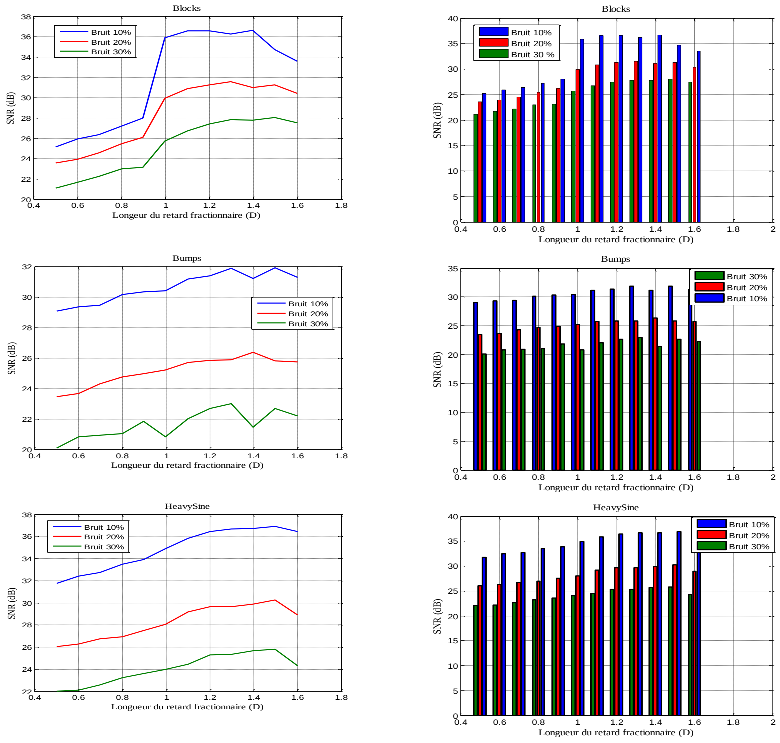

Figure.4SNR Variation as a function of fractional delay length (D).

Table.2 Summary of the Best Signal Denoising Results: Blocks, Bumps and Heavy-sine (Compact Support Fractional Wavelet)

Input signals	*σ/SNR Denoisedsignal*	*SNR of denoised signal*						
Blocks	*σ =10/29.45*	*db2*	*m1=0.1* *m2=0.1* *m3=0.6*	*m1=0.1* *m2=0.1* *m3=1.1*	*m1=0.2* *m2=0.2* *m3=0.4*	*m1=0.2* *m2=0.2* *m3=0.5*	*m1=0.2* *m2=0.2* *m3=1.5*	*m1=0.4* *m2=0.4* *m3=0.6*
		35.80	*36.61*	*36.57*	*36.56*	*36.57*	*36.61*	*36.74*
			m1=0.1	*m1=0.1*	*m1=0.1*	*m1=0.4*	*m1=0.7*	*m1=0.7*

	σ =20/23.46	*db2*	*m2=0.7* *m3=1.7*	*m2=0.8* *m3=1.7*	*m2=0.9* *m3=1.7*	*m2=1.0* *m3=1.1*	*m2=0.8* *m3=1.4*	*m2=0.8* *m3=1.7*
		29.8	*32.02*	*32.17*	*32.05*	*31.96*	*32.04*	*32.13*
	σ =30/19.90	*db2*	*m1=0.1* *m2=0.7* *m3=1.7*	*m1=0.1* *m2=0.8* *m3=1.7*	*m1=0.1* *m2=1.0* *m3=1.7*	*m1=0.2* *m2=0.8* *m3=1.7*	*m1=0.2* *m2=1.0* *m3=1.7*	*m1=0.3* *m2=1.0* *m3=1.7*
		25.84	*30.26*	*30.20*	*30.33*	*30.09*	*30.33*	*29.92*
Bumps	*σ =10/25.10*	*db2*	*m1=0.1* *m2=0.7* *m3=1.4*	*m1=0.1* *m2=0.9* *m3=1.2*	*m1=0.1* *m2=1.0* *m3=1.2*	*m1=0.5* *m2=0.9* *m3=1.7*	*m1=0.5* *m2=1.0* *m3=1.5*	*m1=0.6* *m2=0.8* *m3=1.0*
		29.82	*32.79*	*32.68*	*32.76*	*32.70*	*32.83*	*32.71*
	σ =20/19.09	*db2*	*m1=0.1* *m2=0.8* *m3=1.2*	*m1=0.1* *m2=0.8* *m3=1.7*	*m1=0.2* *m2=0.6* *m3=0.9*	*m1=0.2* *m2=0.7* *m3=0.9*	*m1=0.2* *m2=0.8* *m3=1.6*	*m1=0.3* *m2=0.7* *m3=1.6*
		25.00	*27.26*	*27.35*	*27.26*	*27.34*	*27.38*	*27.35*
	σ =30/15.57	*db2*	*m1=0.1* *m2=0.7* *m3=0.9*	*m1=0.2* *m2=0.6* *m3=1.5*	*m1=0.2* *m2=0.7* *m3=1.5*	*m1=0.2* *m2=0.8* *m3=1.7*	*m1=0.3* *m2=0.8* *m3=1.7*	*m1=0.5* *m2=0.9* *m3=1.7*
		22.01	*24.07*	*24.07*	*24.10*	*24.07*	*24.08*	*24.05*
heavy-sine	*σ =10/29.79*	*db2*	*m1=0.1* *m2=0.7* *m3=1.1*	*m1=0.1* *m2=1.0* *m3=1.6*	*m1=0.1* *m2=1.0* *m3=1.7*	*m1=0.2* *m2=0.8* *m3=1.5*	*m1=0.3* *m2=1.0* *m3=1.5*	*m1=0.3* *m2=1.0* *m3=1.7*
		34.97	*38.90*	*38.90*	*39.00*	*38.94*	*39.19*	*39.23*
	σ =20/23.76	*db2*	*m1=0.2* *m2=0.9* *m3=1.4*	*m1=0.3* *m2=0.8* *m3=1.3*	*m1=0.3* *m2=0.9* *m3=1.2*	*m1=0.3* *m2=0.9* *m3=1.7*	*m1=0.4* *m2=0.8* *m3=1.0*	*m1=0.4* *m2=1.0* *m3=1.5*
		27.89	*32.09*	*32.08*	*31.98*	*31.81*	*31.82*	*32.00*
	σ =30/20.23	*db2*	*m1=0.1* *m2=0.7* *m3=1.1*	*m1=0.2* *m2=0.7* *m3=1.4*	*m1=0.2* *m2=0.8* *m3=1.4*	*m1=0.2* *m2=0.8* *m3=1.7*	*m1=0.2* *m2=1.0* *m3=1.5*	*m1=0.4* *m2=0.8* *m3=1.5*
		23.93	*27.23*	*27.75*	*27.44*	*27.24*	*27.87*	*27.28*

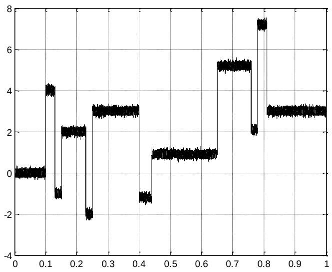

Noisy signal (Blocks 10%)

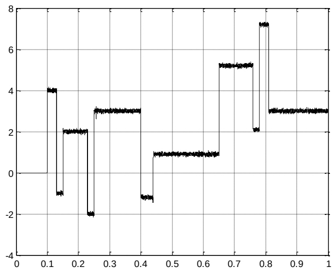

Denoised signal (m1= 0.1 – m2 =0.1 – m3 =0.6)

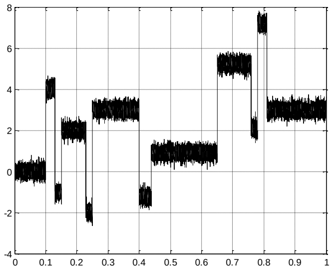

Noisy signal (Blocks 20%)

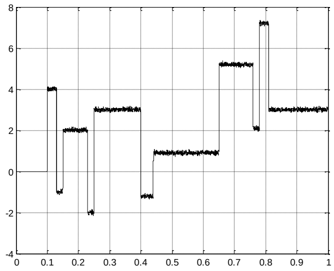

Denoised signal (m1= 0.1 – m2 =0.8 – m3 =1.7)

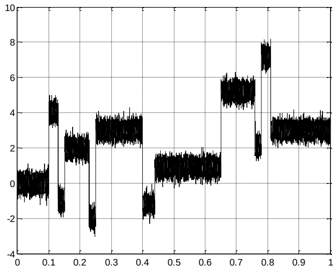

Noisy signal (Blocks 30%)

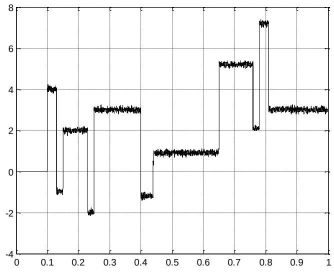

Denoised signal (m1= 0.1 – m2 =1.0 – m3 =1.7)

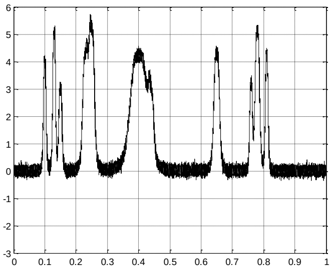

Noisy signal (Bumps 10%)

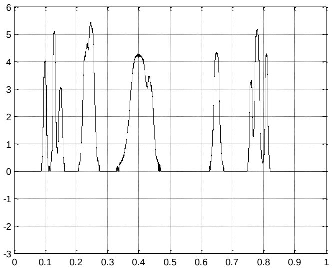

Denoised signal (m1= 0.5 – m2 =1.0 – m3 =1.5)

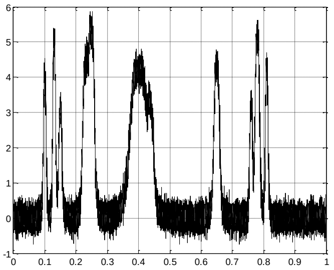

Noisy signal (Bumps 20%)

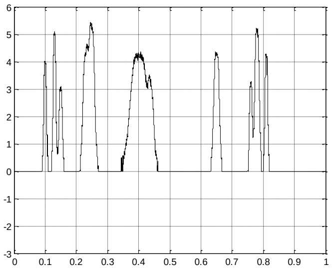

Denoised signal (m1= 0.2 – m2 =0.8 – m3 =1.6)

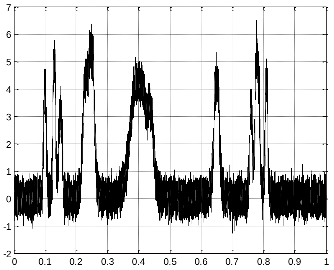

Noisy signal (Bumps 30%)

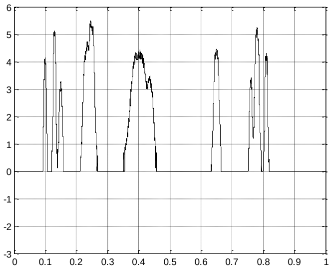

Denoised signal (m1= 0.2 – m2 =0.7– m3 =1.5)

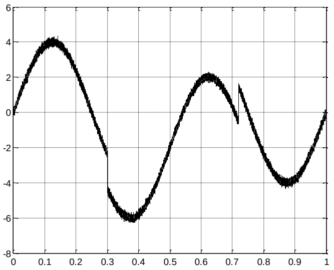

Noisy signal (heavy-sine 10%)

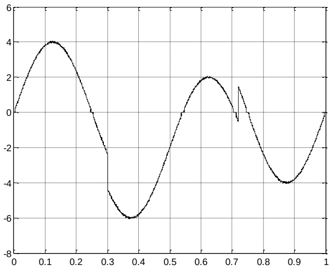

Denoised signal (m1= 0.3 – m2 =1.0 – m3 =1.7)

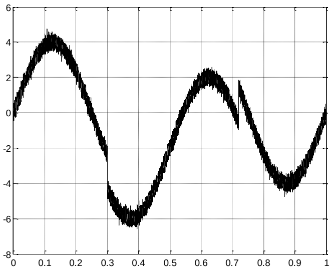

Noisy signal (heavy-sine 20%)

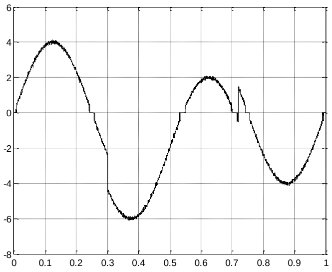

Denoised signal (m1= 0.2 – m2 =0.9 – m3 =1.4)

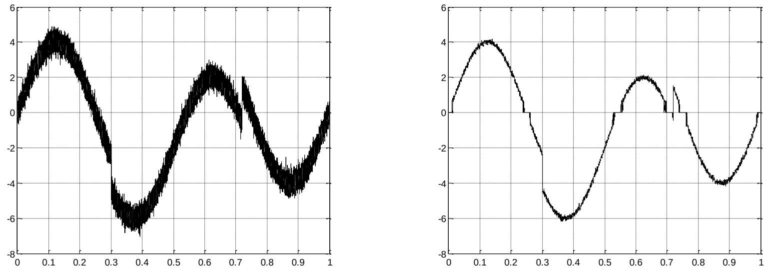

Noisy signal (heavy-sine 30%) *Denoised signal (m1= 0.2 – m2 =1.0 – m3 =1.5)*

Figure 5 Visual Results of Denoised Signals (Compact Support Fractional Wavelets)

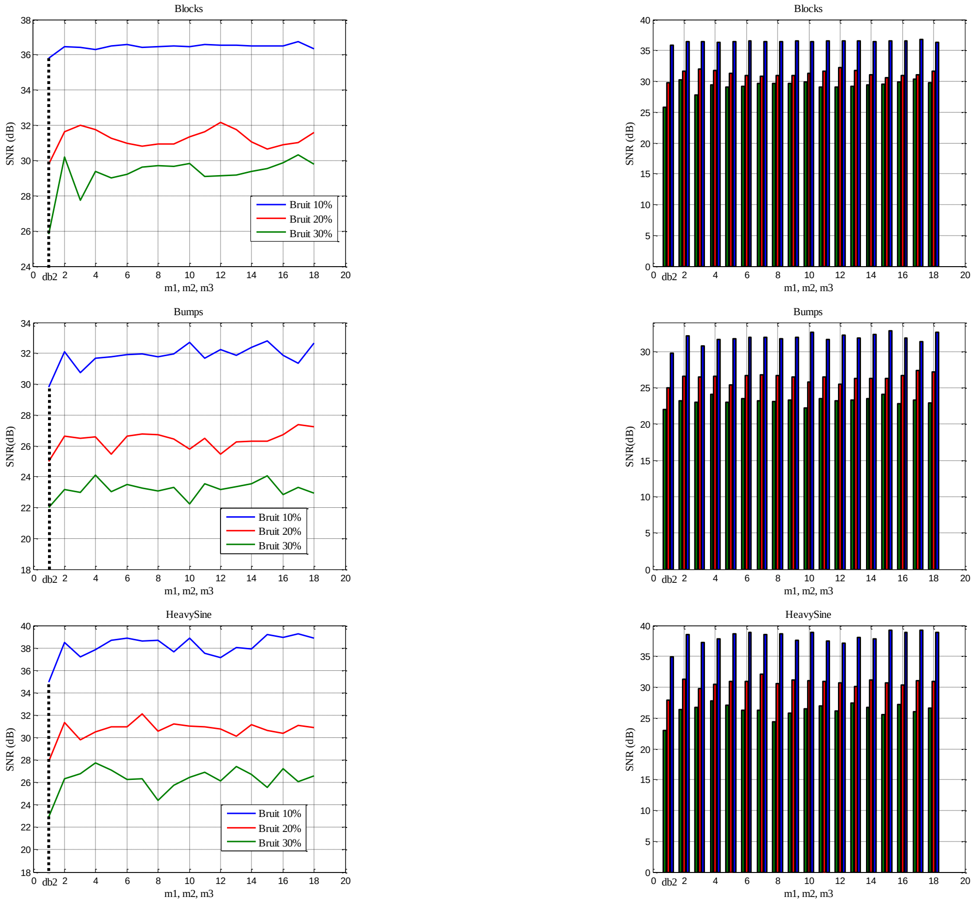

Figure 6 SNR variations as a function of m1, m2 and m3.

VII. Global comparison of signal denoising results

We compare the denoising results obtained previously with the results obtained by applying the most famous wavelets such as: Haar, Daubechies, Coiflettes, Symlettes, Meyer and bi-orthogonal wavelets. By taking into account the same characteristics, in terms of thresholding, type of threshold and level of decomposition, for all wavelets whether fractional or classical. Table 3 summarizes the best results obtained for each type of wavelet. We can see that fractional wavelets produce the best results, compared to other types of wavelets.

Figure 7 presents an overall comparison of the results obtained in the form of histograms. We note that the results of fractional wavelets are much better compared to other types of wavelets especially when it is an intense noise; it comes back to the great flexibility of the filters that constitute them. This important property gives to the fractional wavelets a good selectivity which implies considerable precision especially when decomposing the signals in approximations and details.

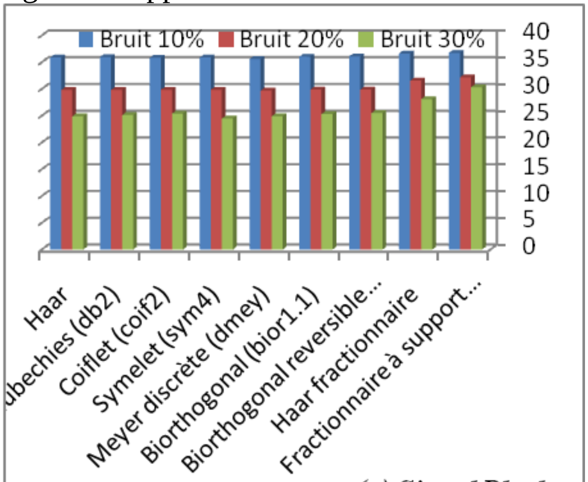

(a) Signal Blocks

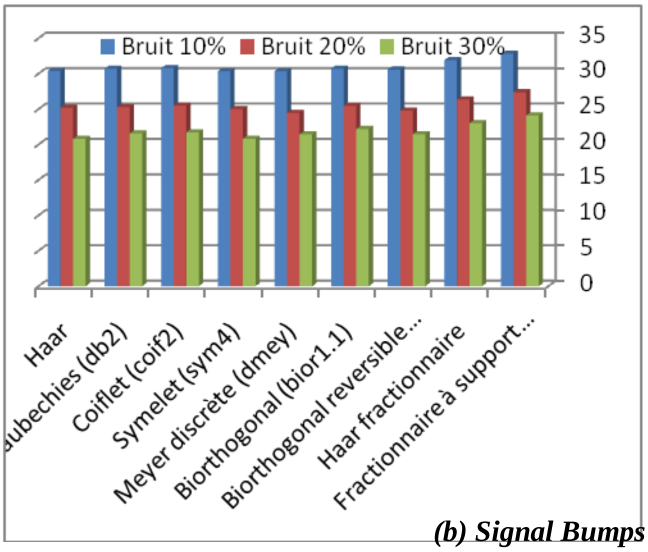

(b) Signal Bumps

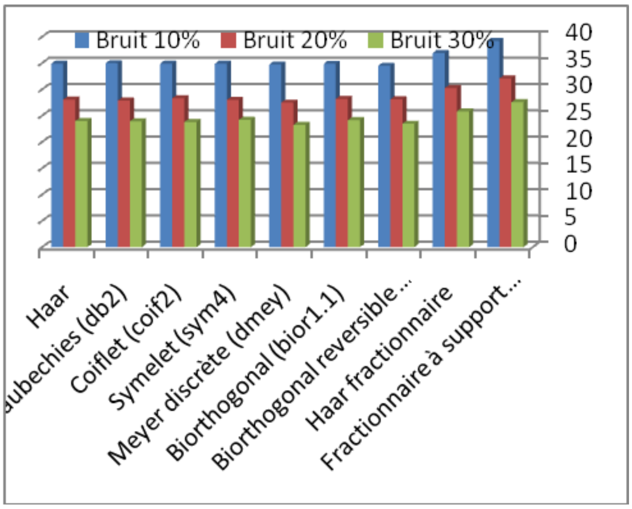

(c) Signal heavy-sin

Figure.7 Global comparison of signal denoising results: (a) Blocks, (b) Bumps, (c) heavy-sin.

Table 3 Overall comparison of signal denoising results: Blocks, Bumps and heavy-sine, using multiple wavelet families.

Input signals	*σ/SNR Denoised signal*	*SNR of Denoised signal*								
		Haar	*db2*	*coif2*	*sym4*	*dmey*	*bior1.1*	*rbio1.1*	*Haarfract.*	*Fract. with compact support*

Blocks	*σ =10 (29.45)*	*35.87*	*35.97*	*35.84*	*35.88*	*35.61*	*36.04*	*36.09*	*36.62*	*36.74*
	σ =20 (23.46)	*29.82*	*29.83*	*29.85*	*29.85*	*29.70*	*29.91*	*29.88*	*31.55*	*32.17*
	σ =30 (19.90)	*24.90*	*25.12*	*25.41*	*24.46*	*24.90*	*25.32*	*25.5*	*28.11*	*30.33*
Bumps	*σ/SNR Denoised signal*									
		Haar	*db4*	*coif3*	*sym4*	*dmey*	*bior2.2*	*rbio1.1*	*Haarfract.*	*Fract. with compact support*
	σ =10 (25.10)	*30.40*	*30.70*	*30.78*	*30.36*	*30.35*	*30.72*	*30.59*	*31.91*	*32.83*
	σ =20 (19.09)	*25.20*	*25.29*	*25.50*	*25.00*	*24.47*	*25.48*	*24.78*	*26.37*	*27.38*
	σ =30 (15.57)	*20.81*	*21.58*	*21.72*	*20.82*	*21.43*	*22.19*	*21.46*	*23.01*	*24.10*
heavy-sine	*σ/SNR Denoised signal*									
		Haar	*db2*	*coif2*	*sym3*	*dmey*	*bior2.2*	*rbio1.1*	*Haarfract.*	*Fract. with compact support*
	σ =10 (29.79)	*34.89*	*34.97*	*34.90*	*34.88*	*34.73*	*34.86*	*34.49*	*36.91*	*39.23*
	σ =20 (23.75)	*28.06*	*27.89*	*28.32*	*28.00*	*27.48*	*28.20*	*28.12*	*30.27*	*32.09*
	σ =30 (20.23)	*23.99*	*23.93*	*23.81*	*24.21*	*23.25*	*24.14*	*23.46*	*25.82*	*27.57*

VIII. Conclusion

We have presented in this paper, one of the applications of the wavelet transform, it is the denoising by thresholding the coefficients of fractional wavelet. We have briefly recalled, in first, the general formalism of the denoising problem as well as the principle of denoising by thresholding the coefficients of wavelet. Then, we implemented the fractional wavelets in a denoising algorithm, as part of a dyadic analysis, a hard thresholding and a SureShrink type threshold, to denoise a set of signals. Experimental results have shown that the performance of fractional wavelets is superior to that of classical wavelets including Haar wavelets, Daubechies, Coiflettes, Symlettes, Meyer and bi-orthogonal wavelets. This performance was observed especially for fractional wavelets with compact support, where we've had very good results. This preference is due to the flexibility, selectivity and high precision of the filters which constitute them.

RÉFÉRENCES

[1] M. Lindenbaum, M. Fischer, and A. M. Bruckstin. On gabor contribution to image enhancement. Pattern Recogition, 27, 1994.

[2] L. Moisan, F. Guichard, and J. M. Morel. A review of p. d. e. models in image processing and image analysis. Journal de Physique, 12:137–154, 2002.

[3] T. F. Chan, J. Shen, and L. Vese.Variationalpde models in image processing. Notices of AMS, 50(1):14–26, 2003.

[4] Li, S. Z. Markov Random Field Modeling in Computer Vision. New York: Springer-Verlag, 1995.

[5] G. Winkler. Image analysis, random fields and dynamic Monte Carlo methods: A mathematical introduction. Springer-Verlag, 1995.

[6] Zhu, S.C., Liu, X.W. and Wu Y.N. Exploring texture ensembles by efficient markov chain Monte Carlo-toward a 'trichromacy' theory of texture. IEEE Transactions on Pattern Analysis and Machine Intelligence, 22(6): 554–569, 2000.

[7] S. Mallat. A theory for multi-resolution signal decomposition: the wavelet representation. IEEE, PAMI, vol. 11, N°7, pp. 674-693, 1989.

[8] L. Boubchir. Approches bayésiennes pour le débruitage des images dans le domaine des transformées multi-échelles

parcimonieuse orientées et non orientées. Thèse doctorat. Université de Caen- Basse Normandie, 2007.

[9] M. Feilner, Mathews Jacob, Michael Unser. Orthogonal quincunx wavelets with fractional orders. Proceedings of the 2001 IEEE International Conference on Image Processing, 2001

[10] Michel Misiti, Yves Misiti, Georges Oppenheim and Jean-Michel Poggi.Wavelets and their applications.ISTE, 2007.

[11] S. Mallat. A Wavelet Tour of Signal Processing.Second edition, Academic Press, 1998.

[12] D. Donoho, I. Johnstone, G. Kerkyacharian, D. picard. Wavelet shrinkage: Asymptopia? J. R. Statist. Soc. B., 57(2): 301–337, 1995.

[13] D. Donoho& I. Johnstone. Ideal Denoising in an orthonormal basis chosen from a library of bases.Department of Statistics. StanfordUniversity, 1994.

[14] S. Mallat. Une exploration des signaux en ondelettes. Editions de l’Ecole Polytechnique, France, 2000.

[15] H. Y. Gao& A. G. Bruce. Waveshrink with firm skrinkage.Static.Sinica, Vol. 7, pp 855–874, 1997.

[16] H. Y Gao. Wavelet shrinkage denoising using the non-negative garrote.Journal of Computational and Graphical Statistics, Vol. 7(4), pp 469–488, 1998.

[17] B, Vidakovic. Statistical Modeling by Wavelets. New York: John Wiley & Sons. 1999.

[18] A. Antoniadis, J. Bigot & T. Sapatinas. Wavelet estimators in nonparametric regression: A comparative simulation study. Journal of Statistical Software, vol. 6(6), pp 1–83, 2001.

[19] Xiao-Ping Zhang. (2001). Thresholding Neural Network for Adaptive Noise Reduction.IEEE Transactions on Neural Networks, vol. 12(3).

[20] D. Donoho, I. Johnstone, G. Kerkyacharian, D. picard. Wavelet shrinkage: Asymptopia? J. R. Statist. Soc. B., 57(2): 301–337, 1995.

[21] D. L. Donoho& I. M. Johnstone. Ideal spatial adaptation by wavelet shrinkage.Biometrika, 81(3):425–455, 1994.

[22] Tao R, Deng B, Wang Y. Research progress of the fractional Fourier transform in signal processing. Sci. China Inf. Sci. Ser. F, vol. 49, pp. 1-25, 2006.

[23] M. Unser, T. Blu. Fractional splines and wavelets.SIAM Review, vol. 42, pp. 43–67, 2000.

[24] F. Abdelliche. Contribution au diagnostic des signaux électrocardiographiques en utilisant les concepts des fractales. Thèse Doctorat, Université Mantouri de Constantine, 2011.

[25] A. Lanani, S. Meghriche, A. Djouambi. Novel design of a fractional wavelet and its application to image denoising.BEEI, vol. 9, 2020.

[26] A. Lanani. Construction d'une Ondelette Fractionnaire Adaptative Appliquée au Traitement de Signal et au Traitement d’Image. Thèse Doctorat, Université Batna 2. 2020

[27] T. I. Laakso, V. Valimaki, M. Karjalainen, U.K. Laine. Splitting the unit delay: tool for fractional delay filter design.IEEE Signal Processing Magazine, vol. 13, pp. 30-60, 1996.

[28] I. Daubechies. Orthonormal bases of compactly supported wavelets. Com. on Pure Appl. Math., vol. 41, pp. 909-996, 1988.

[29] D. Donoho, I. Johnstone, G. Kerkyacharian, D. picard. Wavelet shrinkage: Asymptopia? J. R. Statist. Soc. B., 57(2): 301–337, 1995.

(JMECS) J. Math. Eng. Comp. Sc.
Vol. 00, No. 00, pp. 33-38, (July 2024-Safar 1445$_H$)

The Cauchy Interlace Theorem for Symmetrizable Matrices

Said Kouachi

University Abbes Laghrour, Khenchela, Algeria
E-mail: kouachi@univ-khenchela.dz

Abstract. Symmetrizable matrices are those which are symmetric when multi-plied by a diagonal matrix with positive entries. The Cauchy interlacetheorem states that the eigenvalues of a real symmetric matrix interlacewith those of any principal sub matrix (obtained by deleting a row-columnpair of the original matrix). In this paper we extend the Cauchy interlacetheorem for symmetric matrices to this large class, called symmetrizablematrices or at last we can consider this paper as another proof basedon the celebrated Dodgson's identity [4] . This extension is interestingby the fact that in the symmetric case, the Cauchy interlace theorem together with the Courant-Fischer mini-max theorem and Sylvester's law ofinertia, each one can be proven from the others and thus they are essentially equivalent. The first two theorems have important applications inthe singular value and eigenvalue decompositions, the third is useful inthe development and analysis of algorithms for the symmetric eigenvalueproblem. Consequently various and several applications whom are contingent on the symmetric condition may occur for this large class of notnecessary symmetric matrices and open the door for many applications infuture studies. We recall that our techniques are based on the celebratedDodgson's identity [4].
.

Keywords. Symmetrizable matrices, The Cauchy interlace theorem, Eigenvalues.

AMS Classification.

I. INTRODUCTION

The Cauchy interlace theorem states that the eigenvalues of a real symmetric matrix of order m interlace with those of any principal sub matrix of order m1. The idea behind to extend this theorem to symmetrizable matrices came when we calculated, explicitly, the eigenvalues of a class of m order Tridiagonal, Pentadiagonal and Heptadiagonal matrices (see [10], [13] and [11]) whom are not necessary symmetric but symmetrizable. We observed that their eigenvalues interlace with those of their corresponding m-1 order principal submatrices.We begin by presenting a short and simple proof of the theorem based on the well-knownDodgson's Algorithm, then we prove its extension. At our knowledge, this theorem is applicable only to symmetric matrices and our aim is not to say that our result is new but we hope to provide the reader with another technique to prove the Cauchy interlace theorem.Proofs of this well-known theorem have been based on Sylvester's law of inertia [14], the Courant-Fischer minimax theorem (see [7], [8], [9] and [1]) and others more simple are based on some properties of polynomials [5].

II. THE CAUCHY INTERLACE THEOREM FOR REAL SYMMETRIC MATRICES.

The following theorem presents the more simplified form of the Cauchy interlacetheorem [3].
Theorem 1 (The Cauchy interlace theorem) If a row-column pair is deletedfrom a real symmetric matrix, then the eigenvalues of the resulting matrix interlace those of the original one.

Proof. The celebrated Dodgson's identity [4] states, for a square matrix $A = \left(a_{i,j}\right)_{1\leq i,j\leq m}$, the following

$$\det\left[(a_{i,j})_{1\leq i,j\leq m}\right]\det\left[(a_{i,j})_{\substack{i\neq k,l\\ j\neq k,l}}\right]= \tag{1}$$
$$\det\left[(a_{i,j})_{\substack{i\neq l\\ j\neq l}}\right]\det\left[(a_{i,j})_{\substack{i\neq k\\ j\neq k}}\right]-\det\left[(a_{i,j})_{\substack{i\neq l\\ j\neq k}}\right]\det\left[(a_{i,j})_{\substack{i\neq k\\ j\neq l}}\right],$$

for all $m > 2$. If $\lambda_1 < \lambda_2 < .... < \lambda_m$ lists the eigenvalues of A, then by application of the above identity to the matrix $A-\lambda_p I$ for some fixed $1 \leq p \leq m$, we deduce

$$\det\left[(a_{i,j})_{\substack{i\neq l\\ j\neq l}}-\lambda_p I_{m-1}\right]\det\left[(a_{i,j})_{\substack{i\neq k\\ j\neq k}}-\lambda_p I_{m-1}\right]= \tag{2}$$
$$\det\left[(a_{i,j})_{\substack{i\neq l\\ j\neq k}}-\lambda_p I_{m-1}\right]\det\left[(a_{i,j})_{\substack{i\neq k\\ j\neq l}}-\lambda_p I_{m-1}\right].$$

Since the matrix $A-\lambda_p I$ is symmetric, then

$$\det\left[(a_{i,j})_{\substack{i\neq l\\ j\neq k}}-\lambda_p I_{m-1}\right]=\det\left[(a_{i,j})_{\substack{i\neq k\\ j\neq l}}-\lambda_p I_{m-1}\right], \tag{3}$$

and this shows that all the principal minors of order m-1 of the matrix $A-\lambda_p I$ have the same sign for a fixed $p = 1, \dots m$: By using a well-known properties ofthe characteristic polynomial of the matrix $A-\lambda_p I$ which has p-1 negativeeigenvalues, one null and m -p positive, we deduce that the product Π_{p-1} of the non-zero eigenvalues is equal to the sum of all its principal minors of orderm-1 whom have the same sign as $(-1)^{p-1}$Then, for a fixed $1 \leq k \leq m$, thecharacteristic polynomial of the matrix $\left[(a_{i,j})_{\substack{i\neq k\\ j\neq k}}\right]$

$$P_k(\lambda)=\det\left[(a_{i,j})_{\substack{i\neq k\\ j\neq k}}-\lambda I_{m-1}\right], \tag{4}$$

which is of degree m - 1; satisfies the following inequalities

$$(-1)^{p-1}P_k(\lambda_p) > 0, \qquad p = 1, \dots\dots .. m. \tag{5}$$

This ends the proof of the Cauchy interlace theorem for a real symmetric matrix.

III. Results and Proofs

To introduce the class of matrices (not necessary symmetric) for whom the Cauchy interlace theorem holds, we begin with the following

Definition 2 A square matrix A of order $m > 2$ is called symmetrizable if it is sign symmetric, i.e.

$$a_{ij} = a_{ji} = 0 \ or\ a_{ij}a_{ji} > 0,\ i \neq j = 1,2, \dots\dots .m \tag{6}$$

and if for all permutation σ of the set of integers$\{1,2, \dots\dots m\}$, we have

$$\Pi_{I+1}^{m} a_{i,\sigma_i} = \Pi_{I+1}^{m} a_{\sigma_i,i} \tag{7}$$

When $m = 2$; we simply suppose $a_{12}.a_{21} > 0$ and when $m = 3$, by application of the definition, A is symmetrizable if (6) is satisfied and $a_{12}.a_{23}.a_{31} = a_{21}.a_{32}.a_{13}$; since the other equalities (7) are automatically satisfied. For example, all the matricesare symmetrizable for all real numbers a; b and c

$$A=\begin{pmatrix} a & -3 & 1\\ -6 & b & 4\\ 5 & 10 & c\end{pmatrix}$$

In [6], Lemma 3.2, the authors characterized symmetrizable matrices as follows

Proposition 3 A square matrix of order m is symmetrizable if and only if itis symmetric by sign and for all $k = 3, \dots\dots m$, we have

$$a_{i_1,i_2}.a_{i_2,i_3}\dots a_{i_k,i_1} = a_{i_2,i_1}a_{i_3,i_2}\dots\dots\dots a_{i_1,i_k}$$

for all .nite sequence $i_1, i_2, \dots\dots\dots, i_k$.

However, we present a more simplified version of the above proposition and give the following characterization of symmetrizable matrices.

Proposition 4 A square matrix of order m is symmetrizable if and only if all its principal sub-matrices of order m-1 are symmetrizable.

Proof. First the matrix is symmetric by sign if and only if all its principal sub-matrices are too. If A is symmetrizable, then by choosing in (7) any permutation σ satisfying $\sigma_i = i$, for a fixed $i = 1,2, \dots m$, we can conclude that any principal sub-matrix of a symmetrizable matrix A is also. Supposethat all principal sub-matrices of order $m-1$ are symmetrizable. By writing $i_{k+1} = \sigma(i_k), k = 1, \dots m$ with $i_1 = 1$, then h $i_{m+1} = \sigma_1^m = 1$ and for all $j = 2, \dots m-2$, we have

$$\prod_{l=1}^{m} a_{i,\sigma_i} = \prod_{k=1}^{m} a_{i_k,i_{k+1}} = \left(\prod_{k=1}^{j} a_{i_k,i_{k+1}}\right)\left(\prod_{k=j+1}^{m} a_{i_k,i_{k+1}}\right)$$

Since the (j +1) order principal submatrix with row-column pairs $i_1, i_2, \dots\dots, i_{j+1}$ is symmetrizable, then we have

$$\left(\prod_{k=1}^{j} a_{i_k,i_{k+1}}\right).a_{i_{j+1},i_1} = \left(\prod_{k=1}^{j} a_{i_{k+1},i_k}\right).a_{i_1,i_{j+1}}.$$

Analogously, the (μ □φ) order principal submatrix matrix with row-columnpairsιφ+1; ιφ+2; :::; ιμ; ι1 is symmetrizable, then we have

$$\left(\prod_{k=j+1}^{m} a_{i_k,i_{k+1}}\right).a_{i_1,i_{j+1}} = \left(\prod_{k=j+1}^{m} a_{i_{k+1},i_k}\right).a_{i_{j+1},i_1},$$

then, taking in account that αιφ+1;ι1αι1;ιφ+1 6= o, deduce that

$$\left(\prod_{k=1}^{j} a_{i_k,i_{k+1}}\right)\left(\prod_{k=j+1}^{m} a_{i_k,i_{k+1}}\right) = \left(\prod_{k=1}^{j} a_{i_{k+1},i_k}\right)\left(\prod_{k=j+1}^{m} a_{i_{k+1},i_k}\right)$$

and this gives (7)

Remark 5

It is shown that a matrix A is symmetrizable if and only if there exists a diagonal matrix D with positive entries (called Symmetrizer), such that the matrix D:A is symmetric (see [5]).

Our main result is the following

Theorem 6

The eigenvalues of a real symmetrizable matrix A of order m are all real and interlace with those of any principal sub-matrix of order m - 1.

The proof of the theorem is based on an equality analogous to (3) which is summarized by the following

Lemma 7 For any symmetrizable matrix A, we have

$$a_{lk}.\det\left[(a_{i,j})_{\substack{i\neq l\\ j\neq k}} - \lambda I_{m-1}\right] = a_{kl}.\det\left[(a_{i,j})_{\substack{i\neq k\\ j\neq l}} - \lambda I_{m-1}\right], \qquad (8)$$

For all real λ and all integers $k, l = 1,2,\dots m$

Proof. Simultaneously permuting rows and columns, if necessary, we mayassume that $= 1$; $l = 2$l = 2 and $a_{12}.a_{21} > 0(\,ie \neq 0)$. We should prove thefollowing

$$P(\lambda) = Q(\lambda), \text{ for all real } \lambda, \qquad (9)$$

where

$$P(\lambda) = a_{12}.\det\left[(a_{i,j})_{\substack{i\neq 1\\ j\neq 2}} - \lambda I_{m-1}\right],$$

and

$$Q(\lambda) = a_{21}.\det\left[(a_{i,j})_{\substack{i\neq 2\\ j\neq 1}} - \lambda I_{m-1}\right].$$

The left and right parts of formula (9) can be written, respectively, as follows

$$P(\lambda) = a_{12}.\begin{vmatrix} a_{21} & a_{23} & \cdots & a_{2,(m-1)} & a_{2,m} \\ a_{31} & a_{33}-\lambda & \cdots & a_{3,(m-1)} & a_{3,m} \\ \vdots & \vdots & \ddots & \vdots & \vdots \\ a_{(m-1),1} & a_{(m-1),3} & \cdots & a_{(m-1),(m-1)}-\lambda & a_{(m-1),m} \\ a_{m,1} & a_{m,3} & \cdots & a_{m,(m-1)} & a_{m,m}-\lambda \end{vmatrix}, \qquad (10)$$

and

$$Q(\lambda) = a_{21}.\begin{vmatrix} a_{12} & a_{13} & \cdots & a_{1,(m-1)} & a_{1,m} \\ a_{32} & a_{33}-\lambda & \cdots & a_{3,(m-1)} & a_{3,m} \\ \vdots & \vdots & \ddots & \vdots & \vdots \\ a_{(m-1),2} & a_{(m-1),3} & \cdots & a_{(m-1),(m-1)}-\lambda & a_{(m-1),m} \\ a_{m,2} & a_{m,3} & \cdots & a_{m,(m-1)} & a_{m,m}-\lambda \end{vmatrix}.$$

Since a square matrix and its transpose have the same determinant, then

$$Q(\lambda) = a_{21}.\begin{vmatrix} a_{12} & a_{32} & \cdots & a_{(m-1),2} & a_{m,2} \\ a_{13} & a_{33}-\lambda & \cdots & a_{(m-1),3} & a_{m,3} \\ \vdots & \vdots & \ddots & \vdots & \vdots \\ a_{1,(m-1)} & a_{3,(m-1)} & \cdots & a_{(m-1),(m-1)}-\lambda & a_{m,(m-1)} \\ a_{1,m} & a_{3,m} & \cdots & a_{(m-1),m} & a_{m,m}-\lambda \end{vmatrix}. \qquad (11)$$

As A is symmetrizable, then the matrix $A - \lambda m$and all its principal sub-matrices are symmetrizable for all real λ : By developing the determinants in formulas(10) and (11) each one with respect to its

.rst row for example, we can remarkthat each coefficient in the $(m-2)$ degree polynomial $P(\lambda)$ is equal to its analogous in the expression of the same degree polynomial Q(λ):
Indeed, the coefficient of λ^{m-2} is $(-1)^{m-2}a_{12}.a_{21}$ for both $P(\lambda)$ and $Q(\lambda)$, that of λ^{m-3} is $(-1)^{m-3}\sum\left\|\begin{matrix} a_{21} & a_{2,k} \\ a_{k,1} & a_{k,k}\end{matrix}\right\|$ for $P(\lambda)$ and $(-1)^{m-3}\sum\left\|\begin{matrix} a_{12} & a_{k,2} \\ a_{1,k} & a_{k,k}\end{matrix}\right\|$ for $Q(\lambda)$, whom are equal since the sub-matrices

$$A_k = \begin{pmatrix} a_{11} & a_{12} & a_{1k} \\ a_{21} & a_{22} & a_{2k} \\ a_{k,1} & a_{k1} & a_{kk} \end{pmatrix}$$

are symmetrizable for all $k = 3, \dots m$. For all integer$l \geq 4$, the coefficient ofλ^{m-l} is

$$(-1)^{m-l}a_{12}\sum_{3\leq k_1<k_2<\ldots<k_{l-2}\leq m}\begin{vmatrix} a_{21} & a_{2,k_1} & \cdots & a_{2,k_{l-2}} \\ a_{k_1,1} & a_{k_1,k_1} & \cdots & a_{k_1,1} \\ \vdots & \vdots & \ddots & \vdots \\ a_{k_{l-2},1} & a_{k_{l-2},k_1} & \cdots & a_{k_{l-2},k_{l-2}} \end{vmatrix}$$

for $P(\lambda)$ and

$$(-1)^{m-l}a_{21}\sum_{3\leq k_1<k_2<\ldots<k_{l-2}\leq m}\begin{vmatrix} a_{12} & a_{k_1,2} & \cdots & a_{k_{l-2},2} \\ a_{1,k_1} & a_{k_1,k_1} & \cdots & a_{k_{l-2},k_1} \\ \vdots & \vdots & \ddots & \vdots \\ a_{1,k_{l-2}} & a_{k_1,k_{l-2}} & \cdots & a_{k_{l-2},k_{l-2}} \end{vmatrix}$$

for $Q(\lambda)$, whom are equal since the subamtrices

$$A_{k_1,k_2,\ldots,k_{l-2}} = \begin{pmatrix} a_{11} & a_{12} & a_{1,k_1} & a_{1,k_2} & \cdots & a_{1,k_{l-2}} \\ a_{21} & a_{22} & a_{2,k_1} & a_{2,k_2} & \cdots & a_{2,k_{l-2}} \\ a_{k_1,1} & a_{k_1,2} & a_{k_1,k_1} & a_{k_1,k_2} & \cdots & a_{k_1,k_{l-2}} \\ a_{k_2,1} & a_{k_2,2} & a_{k_2,k_1} & a_{k_2,k_2} & \cdots & a_{k_2,k_{l-2}} \\ \vdots & \vdots & \vdots & \vdots & \ddots & \vdots \\ a_{k_{l-2},1} & a_{k_{l-2},2} & a_{k_{l-2},k_1} & a_{k_{l-2},k_2} & \cdots & a_{k_{l-2},k_{l-2}} \end{pmatrix}$$

are symmetrizable for all $3 \leq k_1 < k_2 < \ldots < k_{l-2} \leq m$. This gives (9) and ends the proof of the Lemma. ∎

Proof. (of Theorem 6) Let $\lambda_1 < \lambda_2 < \ldots < \lambda_m$ the eigenvalues of the symmetrizable matrix A, then by application of the Lemma and taking in account that $a_{lk}.a_{lk} > 0$, for all $k, l = 1, 2, \ldots, m$, we can conclude that the two determinants in (8) have the same sign for a fixed $p = 1, 2, \ldots, m$. The Dodgson's algorithm (1) applied to the matrix $A - \lambda_p I_m$ gives the formula (2) from which we can deduce, in the same way as when the matrix A is symmetric, that all principal minors of order $m-1$ of the matrix $A - \lambda_p I$ have the same sign. The rest of the proof can be obtained by following the same reasoning as in the proof of the Cauchy interlace theorem for symmetric matrices given is the beginning of the above section.

To prove, via the Dodgson's algorithm, that the eigenvalues of the symmetrizable matrix A are all real, we shall do this by induction on m:
For $m = 3$, the Dodgson's algorithm (1) gives

$$\begin{vmatrix} a_{11}-\lambda & a_{12} & a_{13} \\ a_{21} & a_{22}-\lambda & a_{23} \\ a_{31} & a_{32} & a_{33}-\lambda \end{vmatrix}(a_{22}-\lambda) = \begin{vmatrix} \begin{vmatrix} a_{11}-\lambda & a_{12} \\ a_{21} & a_{22}-\lambda \end{vmatrix} & \begin{vmatrix} a_{21} & a_{22}-\lambda \\ a_{31} & a_{32} \end{vmatrix} \\ \begin{vmatrix} a_{12} & a_{13} \\ a_{22}-\lambda & a_{23} \end{vmatrix} & \begin{vmatrix} a_{22}-\lambda & a_{23} \\ a_{32} & a_{33}-\lambda \end{vmatrix} \end{vmatrix}. \tag{12}$$

Let μ_1 and μ_2 the eigenvalues of the submatrix

$$\begin{pmatrix} a_{11} & a_{12} \\ a_{21} & a_{22} \end{pmatrix}.$$

Since $a_{12}a_{21} > 0$, then μ_1 and μ_2 are real and we have

$$\mu_1 < a_{22} < \mu_2. \tag{13}$$

By application of the Lemma, we have

By application of the Lemma, we have

$$\begin{vmatrix} a_{21} & a_{22}-\mu_i \\ a_{31} & a_{32} \end{vmatrix}\begin{vmatrix} a_{12} & a_{13} \\ a_{22}-\mu_i & a_{23} \end{vmatrix} > 0, \ i = 1, \ 2,$$

which gives

$$(a_{22}-\mu_i)\,P_3(\mu_i) < 0, \ i = 1, \ 2,$$

where $P_3(\lambda)$ denotes the characteristic polynomial of A for $m = 3$. Using (13), we deduce that $P_3(\mu_1) < 0$ and $P_3(\mu_2) > 0$. Since $\lim\limits_{\lambda\to-\infty} P_3(\lambda) = +\infty$ and $\lim\limits_{\lambda\to+\infty} P_3(\lambda) = -\infty$, we deduce that $P_3(\lambda)$ has three real roots whom are the eigenvalues of the matrix A when $m = 3$.
Suppose that the eigenvalues of any symmetrizable matrix until the order $m-1$ are real and prove that the property is also true for the order m. By application of The Dodgson's algorithm (1) to the matrix $A - \lambda I_m$ and the formula (8), we have

$$P_m(\lambda)\,.\det\left[(a_{i,j} - \lambda I_{m-2})_{\substack{i\neq k,l\\ j\neq k,l}}\right] \leq \det\left[(a_{i,j} - \lambda I_{m-1})_{\substack{i\neq l\\ j\neq l}}\right]\det\left[(a_{i,j} - \lambda I_{m-1})_{\substack{i\neq k\\ j\neq k}}\right],$$

for all real λ, where $P_m(\lambda)$ denotes the characteristic polynomial of A. Let $\mu_1 < \mu_2 < \ldots. < \mu_{m-1}$ the eigenvalues of $\left[(a_{i,j} - \lambda I_{m-1})_{\substack{i\neq l\\ j\neq l}}\right]$ which is a symmetrizable submmatrix of $A - \lambda I_m$, then

$$P_m(\mu_p)\det\left[(a_{i,j} - \mu_p I_{m-2})_{\substack{i\neq k,l\\ j\neq k,l}}\right] < 0, \ \ p = 1, \ldots, m-1.$$

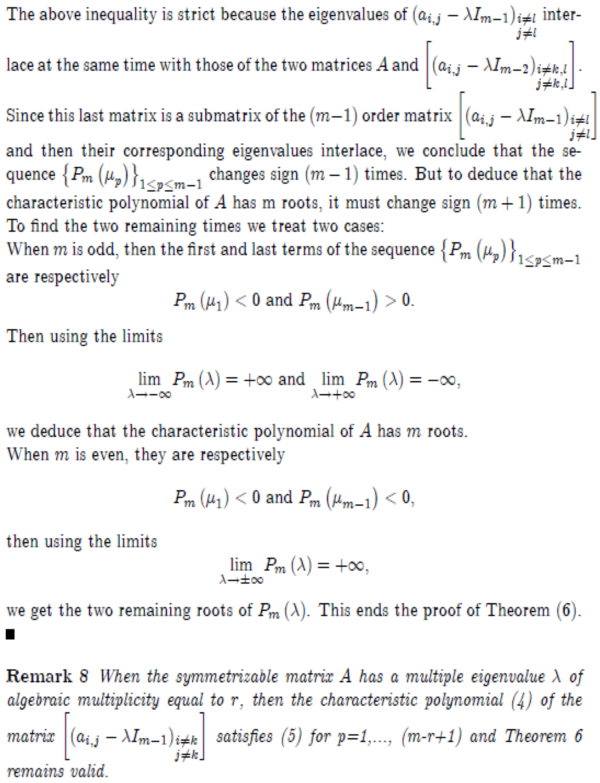

The above inequality is strict because the eigenvalues of $(a_{i,j} - \lambda I_{m-1})_{\substack{i\neq l\\ j\neq l}}$ interlace at the same time with those of the two matrices A and $\left[(a_{i,j} - \lambda I_{m-2})_{\substack{i\neq k,l\\ j\neq k,l}}\right]$. Since this last matrix is a submatrix of the $(m-1)$ order matrix $\left[(a_{i,j} - \lambda I_{m-1})_{\substack{i\neq l\\ j\neq l}}\right]$ and then their corresponding eigenvalues interlace, we conclude that the sequence $\{P_m(\mu_p)\}_{1\leq p\leq m-1}$ changes sign $(m-1)$ times. But to deduce that the characteristic polynomial of A has m roots, it must change sign $(m+1)$ times.
To find the two remaining times we treat two cases:
When m is odd, then the first and last terms of the sequence $\{P_m(\mu_p)\}_{1\leq p\leq m-1}$ are respectively

$$P_m(\mu_1) < 0 \text{ and } P_m(\mu_{m-1}) > 0.$$

Then using the limits

$$\lim_{\lambda\to-\infty} P_m(\lambda) = +\infty \text{ and } \lim_{\lambda\to+\infty} P_m(\lambda) = -\infty,$$

we deduce that the characteristic polynomial of A has m roots.
When m is even, they are respectively

$$P_m(\mu_1) < 0 \text{ and } P_m(\mu_{m-1}) < 0,$$

then using the limits

$$\lim_{\lambda\to\pm\infty} P_m(\lambda) = +\infty,$$

we get the two remaining roots of $P_m(\lambda)$. This ends the proof of Theorem (6).
■

Remark 8 *When the symmetrizable matrix A has a multiple eigenvalue λ of algebraic multiplicity equal to r, then the characteristic polynomial (4) of the matrix $\left[(a_{i,j} - \lambda I_{m-1})_{\substack{i\neq k\\ j\neq k}}\right]$ satisfies (5) for p=1,..., (m-r+1) and Theorem 6 remains valid.*

Acknowledgement 9 The author gratefully acknowledge Qassim University, represented by the Deanship of Scientific Research, on the material support for this research under the number (3388) during the academic year 1436 AH /2015 AD.

References

[1] R. Bellman, Introduction to Matrix Analysis, 2nd ed., McGraw-Hill BookCo., New York, 1970.

[2] D. H. Carlson, On Real Eigenvalues of Complex Matrices, Paci.c Journalof Mathematics, Vol. 15, No. 4, 1965.8

[3] A. Cauchy, Cours d.Analyse de l.EcolePolytechnique,Inoeuvrescompletes,Volumes 2 et 3 (1821).

[4] C.L.Dodgson, Condensation of Determinants, Proc. London Math.Soc.15(1866),150-155.

[5] S. Fisk, A very short proof of Cauchy.s interlace theorem for eigenvalues ofHermitian matrices, arXiv:math/0502408v1 [math.CA]

[6] S. Fomin, A. Zelevinsky, Cluster Algebras II: Finite Type Classi.cation,Invent. Math., (154) 63.121 (2003).

[7] G. H. Golub and C. F. Van Loan, Matrix Computations, 2nd ed., JohnsHopkins University Press, Baltimore, 1989.

[8] R. A. Horn and C. R. Johnson, Matrix Analysis, Cambridge UniversityPress, New York, 1985.

[9] Y. Ikebe, T. Inagaki, and S. Miyamoto, The monotonicity theorem,Cauchy.sinterlace theorem and the Courant-Fischer theorem, Amer. Math.Monthly 94 (1987), no. 4, 352.354. MR 88a:15035. Zbl 623.15010.

[10] S. Kouachi, Eigenvalues and Eigenvectors of Tridiagonal matrices, Electronic Journal of linear Algebra, Vol 15 (April 2006) pp. 115-133.

[11] S. Kouachi, Explicit Eigenvalues of Several Perturbed Pentadiagonal Matrices, Accepted for publication in International Journal of Pure and AppliedMathematics.

[12] S. Kouachi, Eigenvalues and eigenvectors of some tridiagonal matrices withnon-constant diagonal entries, Applicationesmathematicae 35 (1), 107-120.

[13] S. Kouachi, Explicit Eigenvalues of some perturbed Heptadiagonal Matricesvia recurrent sequences, Lobachevskii Journal of Mathematics, Vol. 36,issue 1, pp 28-37(2015).

[14] B. N. Parlett, The Symmetric Eigenvalue Problems, Prentice-Hall, Englewood Cli¤s, NJ, 1980.

JNM: Journal of Natural Sciences and Mathematics
Vol. 9, No. 2, pp. 39-50, (June 2016-Rajab 1437H)

On A Compendious Structure On A Differentiable Manifold

Geeta Verma

Department of Applied Sciences ,Saraswati Institute of Technology & Management , Unnao. (U.P.), INDIA
E-mail : geeta_verma1@yahoo.com

Abstract. In recent years several structures, notable almost contact atructure [2], [6], [8], almost r-contact structure [4],[15], almost paracontact structure [9], almost r-paracontact structure [2], almost contact hyperbolicstructure [14] and almost r-contact hyperbolic structure [5] have been defined and studied on a differentiable manifold by many geometers. Some generalized structures, including almost $(\varepsilon_1, \varepsilon_2)$-contact structure [10], almost $(\varepsilon_1, \varepsilon_2)$-r-contact structure [11], [12] and unified structure [1], [13] have also been defined.

In this paper, We define and study a compendious structure having the following structures as its special cases.

Keywords. compendious structure/integrability and Nijenhuis tensor.

Introduction We first define a compendious structure Σ on a differentiable manifold as follows:

Definition 1 : Let M be an m-dimentional differentiable manifold admitting a tensor field F of type (1,1),linearly independent vector fields (T_x) and 1-form (A_x), x = 1,2,…., r , r < m, such that

$$F(T_x) = 0 \qquad (1)$$

$$F^2 X = ea^r X + cA^r(X)T_x \qquad (2)$$

where e,c take values ± 1 and a^r is a (complex) constant. We define the structure $\Sigma \equiv (F, T_x, A^x)$ to be a compendious structure on M and the pair (M, Σ) or simply M to be a compendious structure manifold.

Agreement 1: In the above and in what follows the indices x,y,z,.... run over (1,2,…..r)

And the equation s containing X,Y,Z,……hold for arbitrary vector fields unless otherwise stated.

Theorem 1 : If M be a compendious structure manifold, then

$$A_x F = 0 \qquad (3)$$

$$A^x(T_y) = -eca^r \delta_y^x \qquad (4)$$

$$\text{rank}(F) = m - r \qquad (5)$$

δ_y^x being Kronecker's symbol.

Now introduce a metric M.

Definition 2 : On a compendious structure manifold (M, Σ) let a metric g be introduced such that

$$g(FX, FY) = a^r g(X,Y) + ec\sum_x A^x(X)A^x(Y) \qquad (6)$$

we define $(\Sigma, g) \equiv (F, T_x, A^x, g)$ to be a compendious metric structure and M equipped with such a metric structure to be a compendious metric structure manifold. The above metric g is said to a metric associated to the compendious structure on M. Setting X=T_x an immediate consequence is that A^x is the covariant form of T_x, that is

$$A^x(Y) = g(T_x, Y) \tag{7}$$

Theorem 2 : On a compendious structure manifold (M, Σ) there always exists a metric g ,given by (6).

Proof : Let h' be any Riemannian metric on M and let h be defined by

$$a^r h(X,Y) \overset{def}{=} -ec\left[h'(F^2X, F^2Y) + \sum_x A^x(X)A^x(Y) \right]$$

Then $h(T_x, Y) = A^x(Y)$ and it is easy to checkthat h is a metric. Now let us defined g by

$$2a^r g(X,Y) \overset{def}{=} h(FX,FY) + a^r h(X,Y) - ec\sum_x A^x(X)A^x(Y)$$

Again g is clearly a metric and the relation

$$\begin{aligned} 2a^r g(FX,FY) &= a^r h(FX,FY) + h(ea^r X + cA^x(X)T_x, ea^r Y + cA^x(Y)T_x) \\ &= a^r h(FX,FY) + a^{2r} h(X,Y) + eca^r \sum_x A^x(X)A^x(Y) \\ &= 2a^{2r} g(X,Y) + 2eca^r \sum_x A^x(X)A^x(Y) \end{aligned}$$

implying (6). However, the metric g is , of course, not unique.

Theorem 3 : On a comoendious metric structure manifold (M, Σ, g) the following relations hold good :

$$g(T_x, FX) = 0 \tag{8}$$

$$g(FX,Y) = eg(X,FY) \tag{9}$$

The proof is obvious.

Using (1) and (2), it is easy to verify the following result.

Theorem 4 : Let (F, T_x, A^x) and $(F, T_x, \bar{A}^x)\left[resp.(F, \bar{T}_x, A^x)\right]$ be two compendious structure on a differentiable manifold M , then we have $A^x = \bar{A}^x\left[resp. T_x = \bar{T}_x\right]$.

Thus we see that two compendious structure having same F and same $(T_x)[resp.(A^x)]$ on a differentiable manifold M always includes another compendious structure on M. So we can prove the following theorem.

Theorem 5 : A compendious structure on a differentiable manifold M is not unique.

Proof : Let H be arbitrary non singular tensor field of type (1,1) on M. Defining

$$\bar{F} \overset{def}{=} H^{-1}FH, \qquad \bar{A}^x \overset{def}{=} A^x H, \qquad \bar{T}_x \overset{def}{=} H^{-1}(T_x) \tag{10}$$

it can easily seen that $(\overline{F},\overline{T}_x,\overline{A}^x)$ is also a compendious structure on M. Moreover if g is an associated metric to the structure (F,T_x,A^x) on M, then a metric $\overline{g}$ on M defined by

$$\overline{g}(X,Y)\overset{def}{=}g(HX,HY) \tag{11}$$

provides an associated metric to the structure $(\overline{F},\overline{T}_x,\overline{A}^x)$ on M.
We can state this fact as foolows.
Corollary (1) : A compendious metric structure on a differentiable manifold is not unique.

Existence of a compendious structure. Let λ be an eigen value of F corresponding to an eigen vector P.We now consider the following two possible cases.
Case I P is linearly independent of (T_x).Then (2) implies that $(\lambda^2-ea^r)P=cA^x(P)T_x$. Hence $\lambda=\pm\sqrt{ea^r}$ and $A^x(P)=0$.

Case II P is a linear combination of (T_x). Then F(P) = 0 that is $\lambda=0$.Therefore, there are r eigen values 0.

Since M is of dimension m and rank(F) = m-r, there are, say, r eigen values 0, s eigenvalues $+\sqrt{ea^r}$ and m-r-s eigenvalues $-\sqrt{ea^r}$. Let L, K and N denote the distributions corresponding to the eigenvalues 0, $+\sqrt{ea^r}$ and $-\sqrt{ea^r}$ respectively.

Lemma(1) The distributions L,K, and N are complementary distributions generated by the complementary projection operators l, k and n defined by

$$l\overset{def}{=}(a^rI-eF^2)a^{-r} \tag{12}$$

$$2k\overset{def}{=}(eF^2+dF)a^{-r} \tag{13}$$

and

$$2n\overset{def}{=}(eF^2-dF)a^{-r} \tag{14}$$

respectively, where I is the identity tensor field and $d=e\sqrt{ea^r}$.
Proof: We see that l+k+n = I.We also have

$$l^2=(a^{2r}I+F^4-2ea^rF^2)a^{-2r}=(a^{2r}I+ea^rF^2-2ea^rF^2)a^{-2r}=l$$

$$k^2=(F^4+d^2F^2+2edF^3)\frac{1}{4}a^{-2r}=(ea^rF^2+ea^rF^2+2da^rF)\frac{1}{4}a^{-2r}=k$$

And similarly $n^2 = n$. Again, we get

$$2lk = (ea^rF^2 + da^rF - F^4 - edF^3)a^{-2r} = (ea^rF^2 + da^rF - ea^rF^2 - da^rF)a^{-2r} = 0$$

$$2l\,n = (ea^rF^2 - da^rF - F^4 + edF^3)a^{-2r} = (ea^rF^2 - da^rF - ea^rF^2 + da^rF)a^{-2r} = 0$$

$$4kn = F^4 - d^2F^2 = ea^rF^2 - ea^rF^2 = 0$$

Consequently *l*, k, n are complementary projection operators. Moreover

$$Fl = (a^rF - eF^3)a^{-r} = (a^rF - a^rF)a^{-r} = 0$$

$$Fk = (eF^3 + dF^2)\frac{1}{2}a^{-r} = (a^rF + e\sqrt{ea^r}F^2)\frac{1}{2}a^{-r} = \sqrt{ea^r}(eF^2 + dF)\frac{1}{2}a^{-r} = k\sqrt{ea^r}$$

and similarly $Fn = -n\sqrt{ea^r}$. We also get $k + n = a^{-r}eF^2$.
Now it remains to show that L, K, and N are the complementary distributions generated by the complementary projection operators l, k, and n that is $L = \{lX; X \in \chi(M)\}$, $K = \{kX; X \in \chi(M)\}$ and $N = \{nX; X \in \chi(M)\}$. Let $Z \in L$.Then, since 0 is the eigen value for L, we have FZ = 0.Also, since Z = *l*Z+kZ+nZ,we get 0 = FZ = FlZ+DkZ+FnZ = 0 + $\sqrt{ea^r}kZ - \sqrt{ea^r}nZ$ or kZ-nZ = 0. But k+n = $a^{-r}eF^2$; therefore kZ+ nZ = 0. Hence kZ = 0 and nZ = 0 and thus Z=*l*Z, that is $L \subset \{lX; X \in \chi(M)\}$.

Conversely, let Z = *l* X, then FZ = F*l*X = 0 which shows that $Z \in L$, that is $\{lX; X \in \chi(M)\} \subset L$. Thus $L = \{lX; X \in \chi(M)\}$.

Again, if $Z \in K$,then since $\sqrt{ea^r}$ is the eigen value for K.We have $\sqrt{ea^r}Z = FZ = FlZ + FkZ + FnZ = 0 + \sqrt{ea^r}kZ - \sqrt{ea^r}nZ$ or Z = Kz – n Z. Also $kZ + nZ = ea^{-r}F^2Z = Z$. Thus Z = k Z, that is $K \subset \{kX; X \in \chi(M)\}$.On the otherhand, let Z = k X, then $FZ = FkX = \sqrt{ea^r}kX = \sqrt{ea^r}Z$. Thus $Z \in K$; that is , $\{kX; X \in \chi(M)\} \subset K$. Hence $K = \{kX; X \in \chi(M)\}$. Similarly, we can prove that $N = \{nX; X \in \chi(M)\}$.

Agreement(2): In what follows the indices $i, j[resp.i', j']$ run over $\{1,......,s\}[resp.\{1,.......,m-r-s\}]$.Now we are in a position to prove the main theorem of this section.

Theorem(6) : A necessary and sufficient condition for M to admit a compendious structure is that there exists complementary projection operators l, k and n which bring together the complementary distributions L, K and N of dimensions r,s and m-r-s respectively, which together span the manifold.

Proof: The necessary part follows from **Lemma(1)**.For sufficient part,let $(T_x, U_i, U_{i'})$ be a set such that (T_x), (U_i) and $(U_{i'})$ are the basis vectors in L,K and N respectively, and let $(-eca^{-r}A^x, V^i, V^{i'})$ be the inverse set.

Therefore, we get

$$\begin{aligned} &-eca^{-r}A^{x}(T_{y})=\delta^{x}_{y},\ A^{x}(U_{i})=0,\ A^{x}(U_{i'})=0, \\ &V^{i}(T_{x})=0, V^{i}(U_{j})=\delta^{i}_{j}, V^{i}(U_{j'})=0 \\ &V^{i'}(T_{x})=0, V^{i'}(U_{j})=0,\ V^{i'}(U_{j'})=\delta^{i'}_{j'} \end{aligned} \tag{15}$$

and

$$V^{i}(X)U_{i}+V^{i'}(X)U_{i'}-eca^{-r}A^{x}(X)T_{x}=X$$

or

$$ea^{r}V^{i}(X)U_{i}+ea^{r}V^{i'}(X)U_{i'}-cA^{x}(X)T_{x}=ea^{r}X \tag{16}$$

$$FX=\sqrt{ea^{r}}V^{i}(X)U_{i}+\sqrt{ea^{r}}V^{i'}(X)U_{i'} \tag{17}$$

we have $F(T_{x})=0$ and

$$\begin{aligned} F^{2}X &=\sqrt{ea^{r}}V^{i}(FX)U_{i}+\sqrt{ea^{r}}V^{i'}(X)U_{i} \\ &=\sqrt{ea^{r}}V^{j}(\sqrt{ea^{r}}V^{i}(X)U_{i}+\sqrt{ea^{r}}V^{i'}(X)U_{i'})U_{j}+\sqrt{ea^{r}}V^{j'}(\sqrt{ea^{r}}V^{i}(X)U_{i} \\ &\quad+\sqrt{ea^{r}}V^{i'}(X)U_{i'})U_{j'} \\ &=ea^{r}V^{i}(X)U_{i}+ea^{r}V^{i'}(X)U_{i'} \\ &=ea^{r}X+cA^{x}(X)T_{x} \end{aligned}$$

Thus (F,T_{x},A^{x}) defines a compendious structure on M.

Integrability Conditions Let us recall some relations of the previous section as follows :

$$lk=kl=ln=nl=kn=nk=o, \tag{18}$$

$$l^{2}=l,\ k^{2}=k,\ n^{2}=n, \tag{19}$$

$$Fl=lF=0 \tag{20}$$

$$Fk=kF=k\sqrt{ea^{r}} \tag{21}$$

$$Fn=nF=-n\sqrt{ea^{r}} \tag{22}$$

$$F^{2}l=0,\ F^{2}k=ea^{r}k,\ F^{2}n=ea^{r}n \tag{23}$$

Lemma (2) : If [F, F] is the Nijenhuis tensor of F, then

$$l[F,F](lX,lY)=0 \tag{24}$$

$$k[F,F](kX,kY)=0 \quad (25)$$

$$n[F,F](nX,nY)=0 \quad (26)$$

$$l[F,F](kX,kY)=ea^{r}l[kX,kY] \quad (27)$$

$$l[F,F](nX,nY)=ea^{r}l[nX,nY] \quad (28)$$

$$k[F,F](lX,lY)=ea^{r}k[lX,lY] \quad (29)$$

$$k[F,F](nX,nY)=4ea^{r}k[nX,nY] \quad (30)$$

$$n[F,F](lX,lY)=ea^{r}n[lX,lY] \quad (31)$$

$$n[F,F](kX,kY)=4ea^{r}n[kX,kY] \quad (32)$$

Proof : The Nijenhuis tensor [F,F] of F is defined by

$$[F,F](X,Y)=[FX,FY]-F[FX,FY]-F[X,FY]+F^{2}[X,Y] \quad (33)$$

But $k+n=e^{-1}F^{2}a^{-r}$, therefore we get

$$[F,F](X,Y)=[FX,FY]-F[FX,Y]-F[X,FY]+ea^{r}k[X,Y]+ea^{r}n[X,Y] \quad (34)$$

On putting in (34) nX and nY in place of X and Y respectively, operating the whole equation by k and using (18), (23), we get (30).
Similarly we get (19)-((29), (31), (32).

Finally , we prove main theorem of this section.

Theorem (7) : The compendious structure manifold M is completely integrable if and only if

$$\begin{aligned}[F,F](X,Y)=[F,F](lX,lY)+[F,F](lX,nY)+[F,F](kX,lY)\\ +[F,F](kX,lY)+[F,F](kX,nY)+[F,F](nX,lY)\\ +[F,F](nX,kY)\end{aligned} \quad (35)$$

Proof: It is well known that any distribution D is integrable if and only if $[X,Y]\in D$ for all $X,Y\in D.$ Thus,the distribution L is integrable if and only if

$$k[lX,lY]=0 \quad (36)$$

$$n[lX, lY] = 0$$
(37)

Equivalently, from (29) and (31), we have

$$k[F,F](lX, lY) = 0$$
(38)

$$n[F,F](lX, lY) = 0$$
(39)

The distribution K is integrable if and only if

$$l[kX, kY] = 0$$
(40)

$$n[kX, kY] = 0$$
(41)

and , equivalently,

$$l[F,F](kX, kY) = 0$$
(42)

$$n[F,F](kX, kY) = 0$$
(43)

Similarly, the distribution N is integrable if and only if

$$l[nX, nY] = 0$$
(44)

$$k[nX, nY] = 0$$
(45)

and equivalently

$$l[F,F](nX, nY) = 0$$
(46)

$$k[F,F](nX, nY) = 0$$
(47)

The Nijenhuis tensor [F,F] of F can be written in the form

$$[F,F](X,Y) = (l+k+n)[F,F]((l+k+n)X, (l+k+n)Y)$$

Expanding right hand and using (24), (26), (38), (39), (40), (41), we get (35).

Special Cases. The structure of this paper generalizes many known structures which may be obtained by taking particular values of a^r, e, c, r. We list these particular cases by giving different values to a^r, e, c, r, writing structural equations corresponding to (2), (4), (6), (9) and discussing the details.

Case 1 : $a^r = 1, e \equiv \varepsilon_1 = \pm 1, c \equiv \varepsilon_2 = \pm 1$). Almost $(\varepsilon_1, \varepsilon_2) - r -$ contact Riemannian structure K.D.Singh and R.K. Agnihotri and R. Singh.

$$F^2 X = \varepsilon_1 X + \varepsilon_2 A^x(X) T_x$$

$$A^x(T_y) = -\varepsilon_1 \varepsilon_2 \delta_y^x$$

$$g(FX, FY) = g(X,Y) + \varepsilon_1 \varepsilon_2 \sum_x A^x(X) A^x(Y)$$

$$g(FX, Y) = \varepsilon_1 g(X, FY)$$

Case 2 : $(a^r = 1, e \equiv \varepsilon_1 = \pm 1, c \equiv \varepsilon_2 = \pm 1, r = 1)$. Almost $(\varepsilon_1, \varepsilon_2) -$ contact Riemannian structure I. Sato.

$$F^2 X = \varepsilon_1 X + \varepsilon_2 A(X) T,$$

$$A(T) = -\varepsilon_1 \varepsilon_2$$

$$g(FX, FY) = g(X,Y) + \varepsilon_1 \varepsilon_2 A(X) A(Y)$$

$$g(FX, Y) = \varepsilon_1 g(X, FY)$$

The existence theorem already has been discussed for cases 1, 2. Now integrability conditions can be deduced from this paper.

Agreement (3) : In the above and in what follows, when $r = 1$, (A^i, T_i) will be identified by (A, T).

Case 3 : $(a^r = 1, e = -1, c = 1)$. Almost r-contact Riemannian structure [4], [7], [15].

$$F^2 X = -X + A^x(X) T_x,$$

$$A^x(T_y) = \delta_y^x$$

$$g(FX, FY) = g(X,Y) - \sum A^x(X) A^x(Y)$$

$$g(FX, Y) = -g(X, FY)$$

Case 4 : $(a^r = 1, e = -1, c = 1, r = 1)$. Almost contact Riemannian structure [2], [6], [8].

$$F^2 X = -X + A(X) T,$$

$$A(T) = 1$$

$$g(FX, FY) = g(X,Y) - A(X) A(Y)$$

$$g(FX, Y) = -g(X, FY)$$

In cases 3, 4 the dimension of K becomes equal to the dimension of N and hence , in case of almost contact manifold, the manifold becomes odd dimensional.

Case 5 : $(a^r = 1, e = 1, c = -1)$. Almost r-paracontact Riemannian structure [3].

$$F^2X = X - A^x(X)T_x,$$
$$A^x(T_y) = \delta^x_y$$
$$g(FX,FY) = g(X,Y) - \sum_x A^x(X)A^x(Y)$$
$$g(FX,Y) = g(X,FY)$$

Case 6 : $(a^r = 1, e = 1, c = -1, r = 1)$. Almost paracontact Riemannian structure [9].

$$F^2X = X - A(X)T,$$
$$A(T) = 1$$
$$g(FX,FY) = g(X,Y) - A(X)A(Y)$$
$$g(FX,Y) = g(X,FY)$$

All the results can be deduced for cases 5,6 by putting appropriate vales for a^r, e, c, r.

Cases 7 : $(a^r = -1, e = -1, c = 1)$. Almost r-contact hyperbolic Riemannian structure [5].

$$F^2X = X + A^x(X)T_x,$$
$$A^x(T_y) = -\delta^x_y$$
$$g(FX,FY) = -g(X,Y) - \sum_x A^x(X)A^x(Y)$$
$$g(FX,Y) = -g(X,FY)$$

Case 8 : $(a^r = -1, e = -1, c = 1, r = 1)$. Almost contact hyperbolic Riemannian structure [14].

$$F^2X = X + A(X)T,$$
$$A(T) = -1$$
$$g(FX,FY) = -g(X,Y) - A(X)A(Y)$$
$$g(FX,Y) = -g(X,FY)$$

To the best of my knowledge , existence and integrability in cases 7, 8 have not studied so far.

Case 9: $(a^r$ replaced by $-a^r, e = -1, c = 1, r = 1)$. Unified metric structure [1] , [13].

$$F^2X = a^rX + A(X)T,$$
$$A(T) = -a^r$$
$$g(FX,FY) = -a^r g(X,Y) - A(X)A(Y)$$
$$g(FX,Y) = -g(X,FY)$$

Putting $(\varepsilon_1, \varepsilon_2) = (-1,1)$, $(\varepsilon_1, \varepsilon_2) = (1,-1)$ and $(\varepsilon_1, \varepsilon_2) = (1,1)$ in case 2 we get almost contact Riemannian structure , almost paracontact Riemannian structure and almost contact hyperbolic structure (but not almost contact hyperbolic Riemannian structure) respectively. In fact , when $(\varepsilon_1, \varepsilon_2) = (1,1)$. we have

$$g(FX,FY) = g(X,Y) + A(X)A(Y), \quad g(FX,Y) = g(X,FY)$$

which does not coincide with the metric of case 8. However, if we take a particular case of the compendious metric structure by setting $a^r = -1$, $e = -1$, $c = 1$, $r = 1$, it would be possible to find an almost contact hyperbolic Riemannian structure [14].

The unified metric structure [1], [13] only unifies an almost contact Riemannian structure [2],[6],[8] and an almost contact hyperbolic Riemannian structure [14]. However, if we take a particular case of compendious metric structure by setting $e = -1$, $c = 1$ and a^r replaced by $-a^r$, it would be possible to find a metric structure which unifies an almost contact Riemannian structure [2],[6],[8] an almost r-contact Riemannian structure [4], [7], [15], an almost contact hyperbolic Riemannian structure [14] and an almost r-contact hyperbolic structure [5].

References

1. **A. Al-Aqeel, A. Hamoui and M.D. Upadhyay :** On algebraic structure manifolds, Tensor (N.S.) 45 (1987), pp. 37-42.

2. **D. E. Blair**: Contact manifolds in Riemannian geometry, Springer Verlag (1976).

3. **A. Bucki** : Almost r-paracontact structure of P-Sasakian type , Tensor (N.S.) 42 (1985), pp. 42-54.

4. **L.S.K. Das**: On almost r-contact metric manifold, C.R. Acad. Sci. Bular.32 (1979), pp.711-714.

5. **K.K Dube and R.Nivas** : Almost r-contact hyperbolic structure in a product manifold, Demonstratio Math.11 (1978), pp. 887-897.

6. **R.S. Mishra**: Structures on a differentiable manifold and their applications, Chandrama Prakashan

7. **R.Nivas and R.Singh**: On almost r-contact structure manifolds, Demonstratio Math.21 (1988), pp.797-803.

8. **S.Sasaki:** On differentiable manifolds with certain structures which are closely related to almost contact structure, I.Tohoku Math.J.12 (1960), pp.456-476 .

9.**I.Sato**: On a structure similar to almost contact structures, Tensor(N.S.) 30 (1976), pp.219-224.

10.K.D. Singh and R.K.Agnihotri: On an almost $(\varepsilon_1, \varepsilon_2)$-contact structure,Demonstratio Math.12 (1979),pp.679-688.

11. R.Singh: Almost $(\varepsilon_1, \varepsilon_2)$ –r-contact manifolds and their product with theEuclidean space E^r,Chapt.8 Ph.D. Thesis Lucknow University,India 1982.

12.K.D. Singh and M.M. Tripathi: On normal $(\varepsilon_1, \varepsilon_2, r)$ almost contact structure.(to appear in Ganita).

13. B.B. Sinha and D.Narain: Integrability condition of C manifold equipped with unified structures,Ganita 38(1987), pp.41-48.

14. M.D.Upadhyay and K.K. Dube: Almost contact hyperbolic (f, g, η, ξ)-structures,Acta Math.Acad.Sci Hungar 28 (1976), pp. 1-4.

15.J.Vanjura: Almost r-contact structure, Ann.Scuola Norm.Sup.Pisa.Sci.Fis. Math. 26 (1972), pp. 75-115.

16. Ram Nivas and Mohd.Nazrul Islam Khan: On Submanifold Immersed in Hsu-Quaternion manifold,The Nepali Mathematical Science report,Vol.21,No.1-2,(2003) pp. 73-79.

الملخص:

(JMECS) J. Math. Eng. Comp. Sc.
Vol. 00, No. 00, pp. 51-60, (July 2024-Safar 1445$_{H}$)

MPPT tracking algorithm based on the Perturbation and Observation method

Abdelkader Saidi[a], Yassine Beddiaf[a,b] and RafikLabdani[a]

[a] University Abbes Laghrour, Khenchela,
E-mail: saidi.abdelkader@univ-khenchela.dz

[b] University of Batna-2, Algeria.

E-mail: beddiaf.yassine@univ-khenchela.dz
E-mail: saidi.abdelkader@univ-khenchela.dz

Abstract. The solar regulator is used in photovoltaic systems to protect the battery against the phenomena of overcharging, and deep discharge. In addition, it ensures the tracking of the maximum power point (MPPT) and allows the photovoltaic generator to deliver its maximum power regardless of the variation in climatic conditions. In this article, we will present an MPPT tracking algorithm based on the Perturbation and Observation method (PO). The idea is to use an adapter boost converter) stage between the photovoltaic Generator (GPV) and the load, the latter is controlled by PWM pulse width modulation using the MPPT algorithm, the simulation results show the feasibility of the proposed algorithm.

Keywords. GPV photovoltaic – MPPT - Boost Converter -.PWM

AMS Classification:

I. INTRODUCTION

The importance of an MPPT regulator in a systemphotovoltaic is no longer to be discussed. He musthowever, be carried out with the greatest care to answerto the requirements of cost, simplicity, and reliability [1].

By definition, an MPPT control, associated with an intermediate adaptation stage, makes it possible to operate a GPV in such a way as to constantly produce the maximum of its power. Thus, whatever the weather conditions (temperature and irradiation), the converter control places the system at the maximum operating point (V_{PM} and I_{PM}). The photovoltaic conversion chain will be optimized through a static converter (SC) controlled by an MPPT [2]. It can be represented by the diagram in Figure (1).

Simulation is an efficient method for evaluating the theoretical performance of various systems. The test equipment may be operated under simply controlled settings, the figure 2 show the chain of solar, we started by the PV, when we use Array type: 1Soltech 1STH-215-P, 1series modules and 1parallel strings, which feeds a resistive load through the Adapter DC-DC boost converter, controlled by an MPPT regulator to extract the maximum power, this panel can be subjected to perturbation from the shading and deflection of the sun.

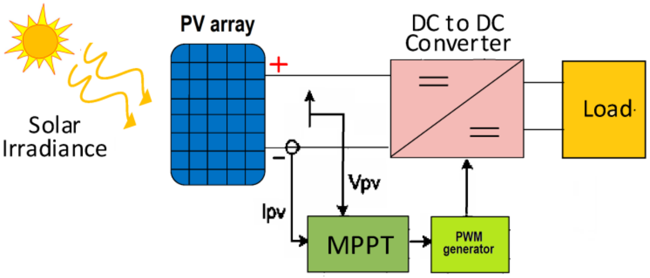

Fig.1 block diagram solar energy chain

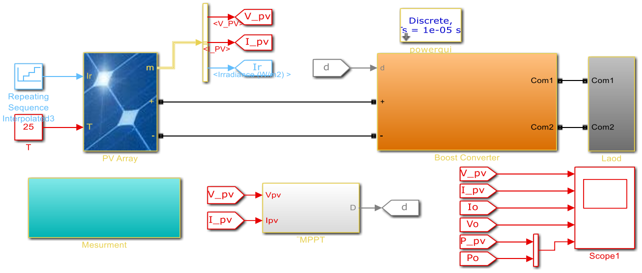

Fig.2Solar chain with Matlab/Simulink

The figure 3 below shows the three algorithms of MPPT

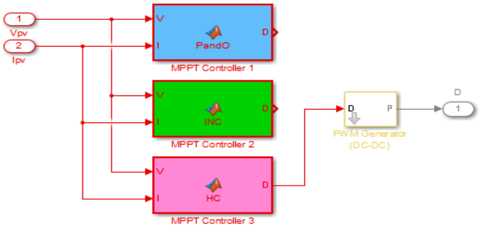

Fig.3Bloc of MPPT technique

II Mathematical Model of the photovoltaic generator

The PV cell is a photodiode, it can be represented by a circuit (Figure 4), and it is the simple model. Taking into account the connection resistances and the leakage currents and starting fromthe ideal model, we can represent a GPV by the diagram, also called the 4parameter model.

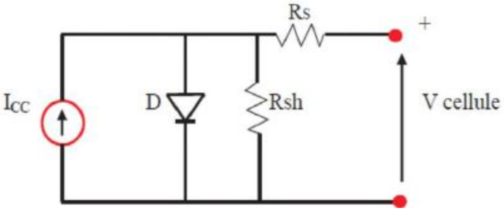

Fig.4Equivalent circuit of the 4 parameter model

The expression of the total current can be expressed by:

$$I = I_{ph} - I_d - I_{sh} \tag{1}$$

The photocurrent I_{ph} proportional to the solar radiation cell,also known as short-circuits currentI_{sc}, $K_o$is the temperature sensitivity, G solar irradiance, and is calculated: [2, 3]

$$I_{sc} = \frac{G}{1000}\left[I_{scr} + K_o(T - T_{ref})\right] \tag{2}$$

The expression of the current diode given:

$$I_d = I_0\left(e^{\frac{q(V+R_sI)}{KT}} - 1\right) \tag{3}$$

Where Io saturation current, q Electron charge (=1.6□10^{-19}C), KBoltzman constant (=1.38□10^{-23} j/k), T temperature cell (K),

The expression of the total current can be expressed by:

$$I = I_S - I_0.e^{\frac{V+R_sI}{V_T}} - \frac{V+R_sI}{R_{sh}} \tag{4}$$

Table 1 Parameters of the PV module

Parameters	***Variable***	***Value***
Maximum power	*P_{MP} (W)*	*213.15*
Open circuit voltage	*V_{oc}(V)*	*36.3*
Short-circuit current	*I_{sc}(A)*	*7.84*
Voltage at maximum power point	*V_{MP} (V)*	*29*
Current at maximum power point	*I_{MP}(A)*	*7.35*
Light-generated current	*I_L (A)*	*7.86*
Shunt resistance	*R_{Sh}(Ω)*	*313.399*
Series resistance	*Rs (Ω)*	*0.39*
Cells per module	*N (Cell)*	*60*

III The influence of irradiation

We save a temperature T = 25 ° C kept constant and we apply irradiation perturbationby vary the sunlight (G) from 200 W/m2 up to 1000 W/m2, the results obtained are illustrated by the following (figures 5).

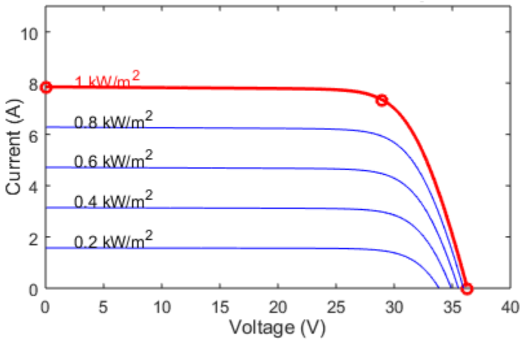

Fig.5 Influence of irradiation on PV current.

IV Boost converter

The mathematical model of the Boost chopper is obtained by applying Kirchhoff's laws to the basic diagram of the chopper, shown in (figure6) and with respect to the operating speed and the condition of switch S. [6]

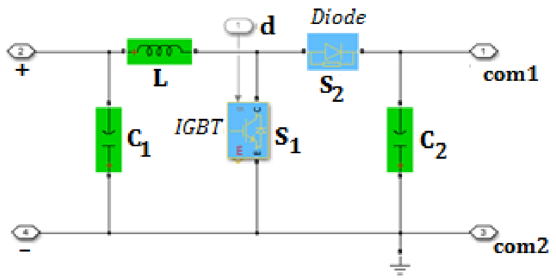

Fig.6 BlockBoost Converter& Switching cycle for DC-DC.

During a period of time T, two switching modes can be expressed (IGBT S1, Diode S2), first mode(S1: ON& S2: OFF),and second mode. (S1: OFF& S2:ON). [7]

$$\begin{cases} L\dfrac{di_L}{dt} = v_{in} - (1-d)v_c \\ C\dfrac{dv_c}{dt} = (1-d)i_L - \dfrac{1}{R}v_c \end{cases} \qquad (5)$$

When v_{in} present the input voltage (V), v_c the output voltage (V), i_L theinductor current (A), and dthe command.

The state equation from (5) is:

$$\begin{bmatrix} \dot{i}_L \\ \dot{v}_C \end{bmatrix} = \begin{bmatrix} 0 & -\dfrac{1}{L}(1-d) \\ \dfrac{1}{C}(1-d) & -\dfrac{1}{RC} \end{bmatrix} \begin{bmatrix} i_L \\ v_C \end{bmatrix} + \begin{bmatrix} \dfrac{1}{L} \\ 0 \end{bmatrix} \begin{bmatrix} v_{in} \end{bmatrix} \qquad (6)$$

Table 2 Parameters of the Boost converter

Parameters	***Variable***	***Value***
Input Capacitor	C_1 (μF)	*100*
Output Capacitor	C_2(μF)	*100*
Inductor	L(mH)	*3*
Switching frequency	f (kHz)	*20*

V RegulatorAlgorithm of MPPT

There are specific control laws to operate the equipment to the maximum of its characteristics, without knowing these points in advance, or without knowing when they are modified, which is the reason for this change. In terms of energy, this translates to the maximum powerpoint. This type of command is commonly referred to in the literature as "Maximum Power Point Tracking" (MPPT). The principle of these controls is to seek the maximum power point (PPM) while ensuring a perfect match between the generator and its load in order to deliver maximum power. This work is devoted to the study of various selected MPPT methods by grouping them according to their principle.

This work is devoted to the study of various selected MPPT methods by grouping them according to their principle. The most commonly encountered are:

- Hill climbing
- Perturb and Observe
- Incremental Conductance

a) Hill climbing (HC)

The Hill Climbing control technique consists in giving a disturbance on the duty cycle which results in a displacement of the operating point along the power-duty cycle characteristic of the photovoltaic generator. Theoretically, research should stop when the maximum power point is reached. [12]

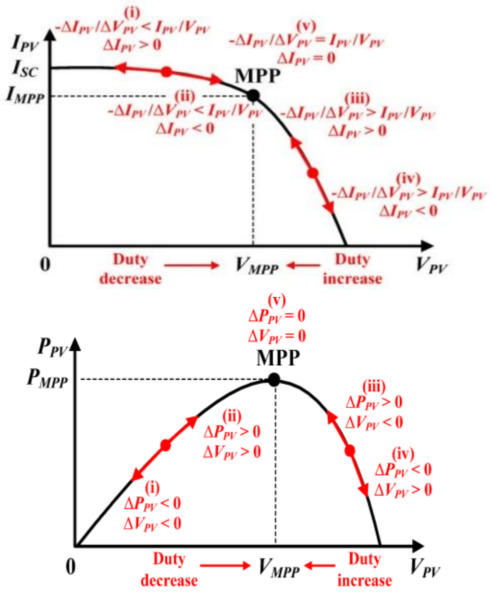

Fig.7 Divergence from MPP &Relationship between power and duty cycle.[12, 13]

More clearly, its working principle consists on periodically measuring PV voltage (Vpv) and current (Ipv), for calculating present PV power (Ppv) and then, a perturbation in the duty ratio (D) of the DC/DC converter is applied, so that its direction makes the operation point approach the MPP [15,16]. The modification of duty cycle directly affects Ipv value, which consequently changes the Vpv [10]. The perturbation direction depends on the comparison of current and just earlier measurement of Ppv, and it has axed step-size.

The Figure8shows the Hill climbing (HC) algorithm.

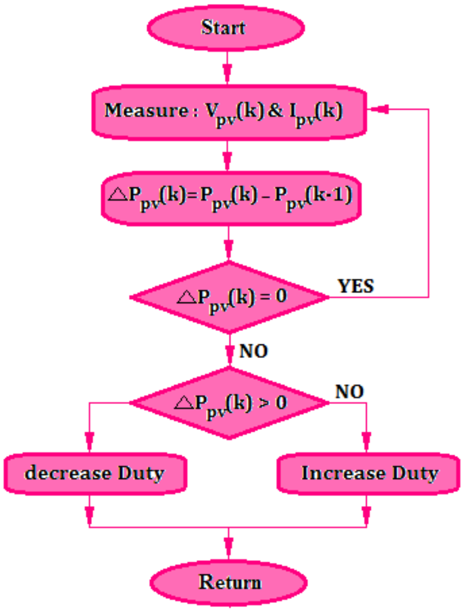

Fig. 8 Flowchart of conventional Hill Climbing (HC) MPPT

In HC, at each iteration *i*, the algorithm starts sensing the voltage, V(*i*) and current, I(*i*) of PV array and the corresponding power, P(*i*)= V(*i*)×I(*i*) is then calculated. Next, the duty cycle (D) of the converter is perturbed by an increment of duty cycle step size (D_{step}), and the resulting change of power, ΔP = P(*i+1*) - P(*i*) is obtained. If the ΔP is positive, then perturbation is in the right direction, and more perturbation is applied in the same direction to reach the MPP. The perturbation direction is reversed if ΔP is negative, an indication that the tracking is moved away from the MPP.[11]

b) Perturbation And Observation method(P&O)

The P&O method is generally the most used because of its simplicity and ease of implementation. As its name suggests, this method is based on the disturbance (an increase or decrease) of the voltage V_{ref}, or of the current I_{ref}, and the observation of the consequence of this disturbance on the measured power (P = V.I). [12]

Its working principle is based on the disturbance of the operating point (by increasing or decreasing the operating voltage) and the observation of its effect on the power (P). If the power increases (ΔP> 0), we are therefore in the right direction, we continue the disturbance in the same direction otherwise (ΔP<0), so we move away from the PPM, we reverse the disturbance. Figure 9 illustrates its principle of operation.

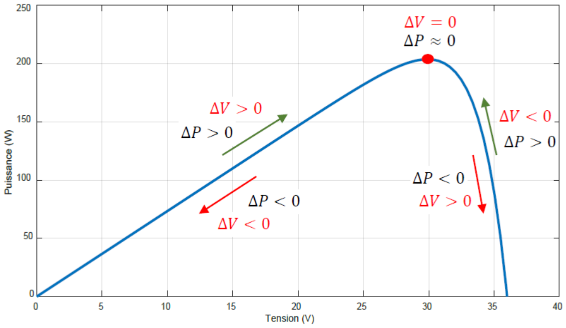

Fig.9 Principle of MPPT with the P&O method [26]

More clearly the operation principle is based on periodical perturbation on the terminal voltage of the PV module and comparison between the current power value of the PV output and the power at the previous perturbation.

Fig. 10 Flowchart of the Perturb and Observe (P&O)

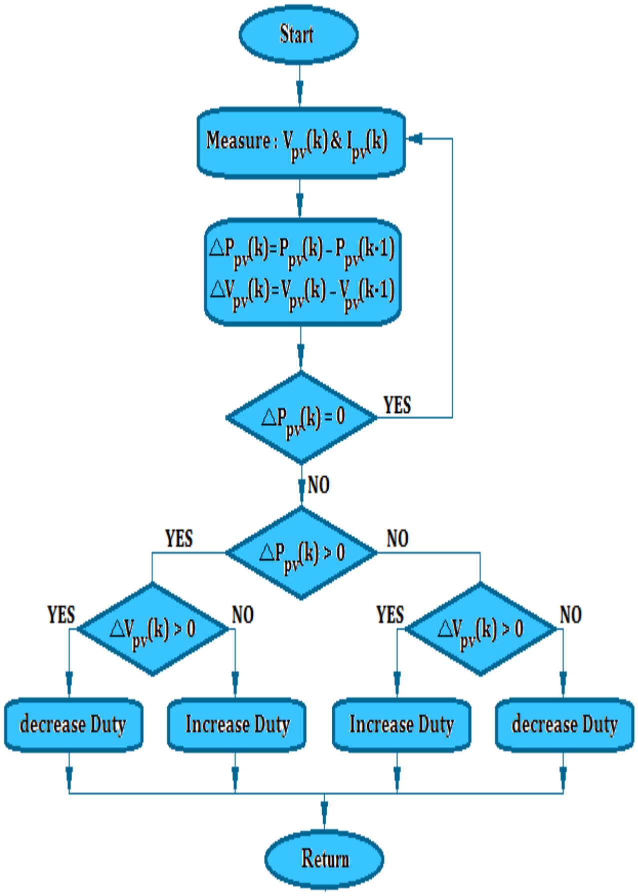

The flowchart of this method is given in Figure 10. We recover the current and the PV voltage then we calculate the new power P(t) and the variation of the voltage (Δv), if the power has increased (ΔP> 0) we are therefore in the right direction, we continue thus d " increase V (if Δv> 0) or continue to decrease it (if Δv<0), otherwise (ΔP<0) it is necessary to invert (increase V if Δv<0 and decrease if ΔV> 0). [13]

c) Incremental Conductance (INC):

The Incremental Conductance method is generally the most used because of its simplicity and ease of implementation. This technique is based on the variation of the conductance of the GPV and its influence on the position of the operating point. [14, 15]

The photovoltaic module's conductance is determined by the ratio of the GPV's current and voltageand the derivative of the power $\frac{dP_{pv}}{dV_{pv}}$ can be described by the following equation

$$\frac{dp_{pv}}{dV_{pv}} = I_{pv} + V_{pv}\frac{dI_{pv}}{dV_{pv}} \approx I_{pv} + V_{pv}\frac{\Delta I_{pv}}{\Delta V_{pv}} \qquad (7)$$

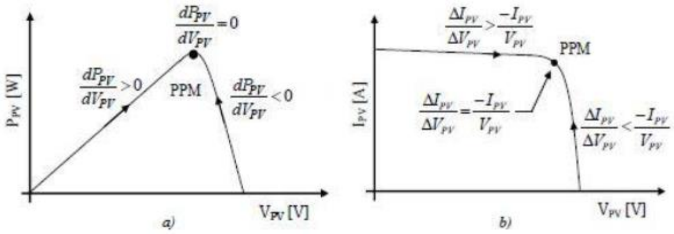

Fig. 11positioning of the operating point according to the sign of the derivative of the conductance G.

The position of the operating point relative to the PPM is determined by the development of the power of the GPV in relation to the voltage, as shown below:

- If $\frac{dP_{pv}}{dV_{pv}}=0$, the operating point is on the PPM
- If $\frac{dP_{pv}}{dV_{pv}}>0$, the operating point is to the left of the PPM
- If $\frac{dP_{pv}}{dV_{pv}}<0$, the operating point is on the right of the PPM

We can write a new condition on the variation of conductance:

- If $\frac{\Delta I_{pv}}{\Delta V_{pv}}=-\frac{I_{pv}}{V_{pv}}$, the operating point is on the PPM.
- If $\frac{\Delta I_{pv}}{\Delta V_{pv}}>-\frac{I_{pv}}{V_{pv}}$, the operating point is to the left of the PPM.
- If $\frac{\Delta I_{pv}}{\Delta V_{pv}}<-\frac{I_{pv}}{V_{pv}}$, the operating point is on the right of the PPM.

The maximum power can then be tracked by making comparisons at each moment of the value of the conductance $\frac{I_{pv}}{V_{pv}}$ with that of the conductance increment $\frac{\Delta I_{pv}}{\Delta V_{pv}}$, as illustrated by the algorithm in Figure (12).

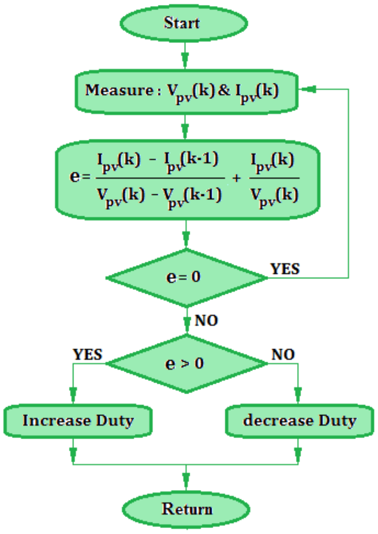

Fig. 12Flowchart Conductance Increment (INC) of MPPT

VI SIMULATION RESULTS:

Figures(13, 14, 15) shows the tracking of Maximum power point, load voltage(Vo), load current(Io), power (Po), and power of the PV array, and efficiencyof system using the conventional Inc. conductance, P&O, and HC algorithm for a sudden increase or decrease in the irradiance. Initially, the PV array is simulated at irradiance of 1000W/m^{2}as shown Figure 13. Hence, INC conduction algorithm start the exploration process to search the MPP at point t=0.601s (Vo=70V, Io= 2.46A, Po= 150W) for irradiation Ir=800W/m^2.

Aftert=0.801s instant, the irradiance is gradually decreased from 800W/m^2 to 300 W/m^2, showing in Figure 14.

Likewise, the same is true for the P&O and H. climbing algorithmin figure (15, 16), except for some oscillations, which determine the efficiency of one of these algorithms.

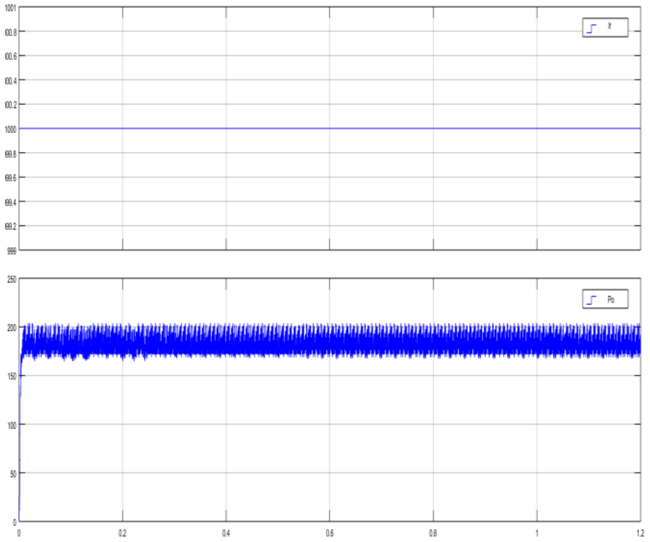

Fig. 13 load power Po with fixed Ir =1000 w/m^2.

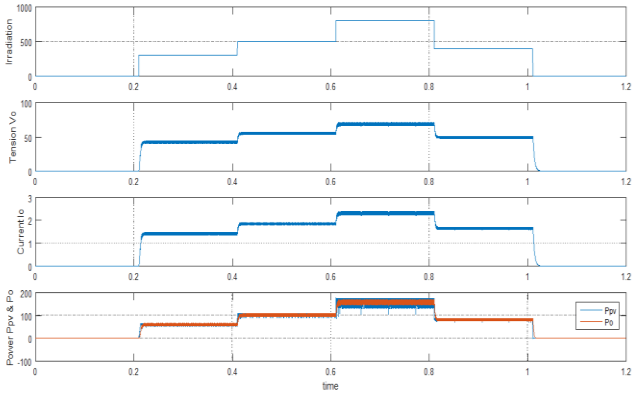

Fig. 14 load current, load voltage, and power under varying weather conditions for INC. Conductance MPPT.

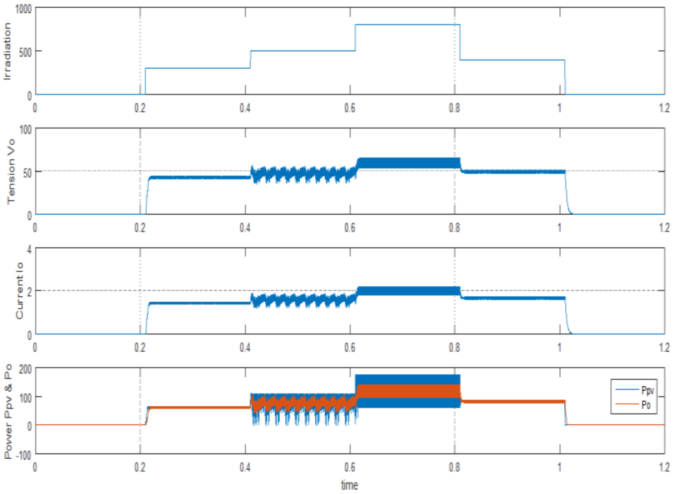

Fig. 15 load current, load voltage, and power under varying weather conditions for P &O MPPT

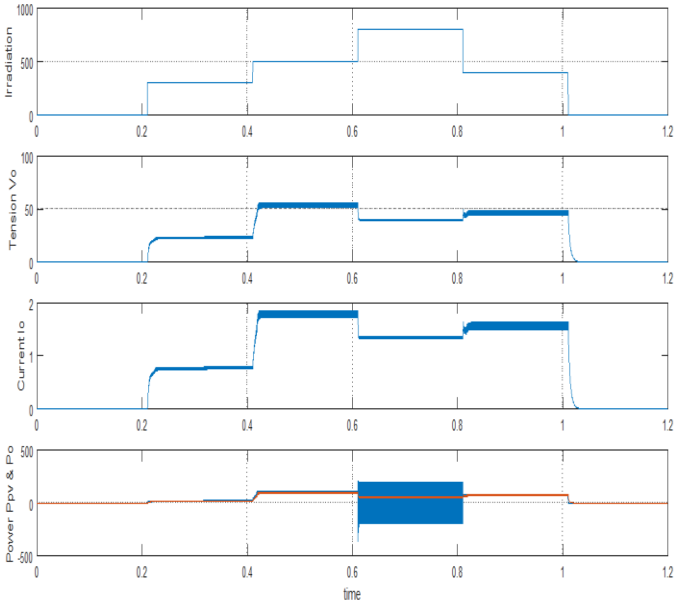

Fig. 16 load current, load voltage, and power under varying weather conditions for HC MPPT.

This work presents the results obtained by three methods of controlling MPPT applied to a PV generator. The work was carried out under the MATLAB/SIMULINK environment.

We count two scenarios: ideal atmospheric conditions (25° and 1000 w/m2) and partial shade. We performed a comparative study between three MPPT methods, the first is the INC method, the second is the P&O method and the third is the HC.

Under standard atmospheric conditions, all three methods give fairly good results. However, from the results obtained, in partial shading, the INC presents very competitive results compared to the other two methods, but does not lead to the maximum extraction of the power.

VII CONCLUSION

Based on the simulation findings, this idea merits additional investigation and should be realized through the practical implementation that we are now working on, which may serve as a basis for future publication and contribution.

Even though, there are no great differences that can be found since the ideal method has not been found yet, which gets maximum power at every time, with much higher efficiency acting with a low time response and an acceptable complexity. Many MPPT methods continue to develop, some methods are named in this work, and many others can be found.

REFERENCES

[1] AngalaesWari.S, Jamuna.K,SanjeevikumarPadmanaban, Baseem Khan, "Design and implementation of a robust of iterative learning controller for voltage and frequency stabilization of hybrid microgrids ", Computer & Electrical Engineering, 84(2);106631,DOI: 10.1016/j.compeleceng.2020.106631.

[2] W. Xiao, N. Ozog, and W. G. Dunford, " Topology Study of Photovoltaic Interface for Maximum Power Point Tracking", IEEE Trans, on Industrial Electronics, vol. 54,n°. 3, 2007, pp. 1696-1704.

[3] M. Kamran, M. Mudassar, M. RayyanFazal, M. Asghar, M. Bilal, R. Asghar, "Implementation of improved Perturb & Observe MPPT

technique with confined search space for standalone photovoltaic system”, Journal of King Saud University – Engineering Sciences, 2018.

[4] A. Bouchakour, L. Zaghba, M. Brahami, and A. Borni, “Study of a Photovoltaic System Using MPPT Buck-BoostConverter”, International Journal of Materials, Mechanics and Manufacturing,Vol. 3, No. 1, February 2015.

[5]H. SAHRAOUI , L. CHRIFI-ALAOUI , S. DRID , P. BUSSY, " Second Order Sliding Mode Control of DC-DC Converter used in the Photovoltaic System According an Adaptive MPPT ", International journal of renewable energy research, Vol.6, No.2, 2016.

[6] A. Jaafar, ‘’Contribution à la modélisation, l'analyse et l'optimisation de lois de commande pour convertisseurs DC-DC de puissance’’, Thèse de doctorat, Soutenue le 14 novembre 2011.

[7] Asma MERDASSI, ’’Outil d’aide à la modélisation moyenne de convertisseurs statiques pour la simulation de systèmes mécatroniques’’, Institut National Polytechnique de Grenoble - INPG, 2009.

[8] André C., Gabriel A, Bruno J, René Z, ‘’ Ingénierie de la commande des systèmes’’, Ellipses Edition Marketing S.A., 2001, ISBN 2-7298-0498-6.

[9] Eltawil, M. A., & Zhao, Z, MPPT techniques for photovoltaic applications. Renewable and Sustainable Energy Reviews, 25, 793-813. (2013).

[10] N. Hashim , Z. Salam , D. Johari , N. Fasdi N. Ismail, " DC-DC Boost Converter Design for Fast and Accurate MPPT Algorithms in Stand-Alone Photovoltaic System " Int J PowElec&DriSyst, Vol. 9, No. 3, September 2018 : 1038 – 1050.

[11] HajarBagheri, “advances in electric power engineering”, publisher: lulu (usa), 2015.

[12] H.Slimane " Optimisation de la conversion énergétique pour les systèmes à énergie Photovoltaïque " Thèse Doctorat en Sciences Université Ferhat Abbas Sétif 1 Faculté de Technologie 10 octobre 2018.

[13] J.H.Lee, H.B.Bo, H.Cho, “Advanced incremental conductance MPPT algorithm with a variable step size”, Power Electronics and Motion Control Conference,12th International, pp. 603-607, Aug. 2006.

[14] T.Y.Kim, H.G.Ahn, S.K. Park, Y.K.Le, ”A novel maximum power point tracking control for photovoltaic power system under rapidly changing solar radiation”, IEEE International Symposium on, Vol. 2, pp. 1011-1014, Jun. 2001.

[15] Dr. B.LALOUNI Sofia " Cours Energie Solaire Photovoltaïque " Université A.MIRA de BEJAIA Faculté de Technologie 2014/2015.

[16] A.Mohamed "Contribution à l‘optimisation d‘une chaine de conversion d‘énergie photovoltaïque", Thèse Doctorat en Sciences en électrotechniqueUniversité Constantine 1 Faculté de Technologie de la technologie .02 / 03 / 2014.

مجلة الرياضيات، الهندسة والإعلام الآلي

Journal of Mathematics, Engineering and Computer Sciences JMECS

Vol. 00, No. 00, July 2024-Safar 1445

CONTENTS

Abbes Laghrour Khenchela University Publications

مجلة علمية محكمة تصدرعن جامعة عباس لغرور خنشلة